The Astrophysical Journal, 626:12–30, 2005 June 10
© 2005. The American Astronomical Society. All rights reserved. Printed in U.S.A.

THE SUNYAEV-ZEL'DOVICH EFFECT IN CMB-CALIBRATED THEORIES APPLIED TO THE COSMIC BACKGROUND IMAGER ANISOTROPY POWER AT $l > 2000$

J. R. Bond,[1] C. R. Contaldi,[1] U.-L. Pen,[1] D. Pogosyan,[2] S. Prunet,[3] M. I. Ruetalo,[1,4]
J. W. Wadsley,[5] P. Zhang,[1,4] B. S. Mason,[6,7] S. T. Myers,[8] T. J. Pearson,[6]
A. C. S. Readhead,[6] J. L. Sievers,[6] and P. S. Udomprasert[6]
Received 2002 May 23; accepted 2005 February 9

ABSTRACT

We discuss the nature of the possible high-l excess in the cosmic microwave background (CMB) anisotropy power spectrum observed by the Cosmic Background Imager (CBI). We probe the angular structure of the excess in the CBI deep fields and investigate whether it could be due to the scattering of CMB photons by hot electrons within clusters, which is the Sunyaev-Zel'dovich (SZ) effect. We estimate the density fluctuation parameters for amplitude, σ_8, and shape, Γ, from CMB primary anisotropy data and other cosmological data. We use the results of two separate hydrodynamic codes for ΛCDM cosmologies, consistent with the allowed σ_8 and Γ values, to quantify the expected contribution from the SZ effect to the band powers of the CBI experiment and pass simulated SZ effect maps through our CBI analysis pipeline. The result is very sensitive to the value of σ_8 and is roughly consistent with the observed power if $\sigma_8 \approx 1$. We conclude that the CBI anomaly could be a result of the SZ effect for the class of ΛCDM concordance models if σ_8 is in the upper range of values allowed by current CMB and large-scale structure data.

Subject headings: cosmic microwave background — cosmology: observations

1. INTRODUCTION

The Cosmic Background Imager (CBI) provides some of the highest resolution observations of the cosmic microwave background that have been made thus far. The observations cover the multipole range $400 < l < 4000$, which corresponds to collapsed masses ranging from a factor of 10 larger than the Local Group to the largest superclusters. These observations show, for the first time, the fluctuations on scales that gave rise to galaxy clusters and the damping of the power on small scales (Silk 1968; Peebles & Yu 1970; Bond & Efstathiou 1987). Together with the results of other recent, high-precision CMB experiments (Miller et al. 1999; Netterfield et al. 2002; Lee et al. 2001; Halverson et al. 2002), the observations fit the scenario of adiabatic fluctuations generated by a period of inflationary expansion. The CBI observations also provide a unique insight into angular scales in which secondary anisotropy effects are thought to become an important contributor to the power spectrum.

In a series of papers, we have presented the results from the first year of CMB observations carried out by the CBI between 2000 January and December. A preliminary analysis of the data was presented in Padin et al. (2001, hereafter Paper I). In Mason et al. (2003, hereafter Paper II), the observations of three differenced $45'$ (FWHM) deep fields were used to measure the power spectrum to multipoles $l \lesssim 3500$ in wide bands $\Delta l \sim 600$. Pearson et al. (2003, hereafter Paper III), discussed the analysis of three sets of differenced $145' \times 165'$ mosaicked fields. Mosaicking gives a telescope a larger effective primary beam than that defined by the dish radii. This increases the resolution in the u-v plane because of the smaller width of the convolving function. It also reduces the effect of cosmic variance on the errors by increasing the sampled area. The mosaic fields provide high signal-to-noise ratio measurements of the power spectrum up to multipoles $l \sim 1700$ with a resolution $\Delta l = 200$. Myers et al. (2003, hereafter Paper IV), give a detailed description of our correlation analysis and band power estimation methods. These have enabled us to analyze efficiently the large data sets involved in the CBI measurements. The implications of the results on cosmological parameters are described in Sievers et al. (2003, hereafter Paper V).

Results from the deep field observations show a fall in the power spectrum up to $l \sim 2000$, which is consistent with the damping tail due to the finite width of the last scattering surface. Beyond $l \sim 2000$, the power observed is higher than that expected from standard models of damped adiabatic perturbations, which provide excellent fits to the data at larger scales. An extensive set of tests have been carried out to rule out possible systematic sources of the measured excess (Paper II). Paper III also reports results in this l-range that are consistent with those of Paper II. Since the thermal noise levels in the CBI mosaic are substantially higher in this regime than in the deep field observations, the current discussion focuses on the deep field results.

The deep field spectrum shows the power dropping to $l \sim 2000$, beyond which power levels are significantly higher than what is expected on the basis of standard models for intrinsic CMB anisotropy. Assuming a single bin in flat band power above $l = 2010$, the observed signal is inconsistent with zero and best-fit models at the 3.5 and 3.1 σ levels, respectively. The 1 and

[1] Canadian Institute for Theoretical Astrophysics, 60 St. George Street, Toronto, ON M5S 3H8, Canada.
[2] Department of Physics, University of Alberta, Edmonton, AB T6G 2J1, Canada.
[3] Institut d'Astrophysique de Paris, 98bis Boulevard Arago, F-75014 Paris, France.
[4] Department of Astronomy and Astrophysics, University of Toronto, 60 St. George Street, Toronto, ON M5S 3H8, Canada.
[5] Department of Physics and Astronomy, McMaster University, Hamilton, ON L8S 4M1, Canada.
[6] California Institute of Technology, 1200 East California Boulevard, Pasadena, CA 91125.
[7] National Radio Astronomy Observatory, P.O. Box 2, Green Bank, WV 24944.
[8] National Radio Astronomy Observatory, P.O. Box O, Socorro, NM 87801.

2 σ confidence intervals for this band power are 359–624 and 199–946 μK^2, respectively, with a best-fit power level of 508 μK^2. The confidence limits were obtained by explicitly calculating the asymmetric, non-Gaussian likelihood of the high-l band power.

A key consideration in obtaining these results is the treatment of the discrete radio source foreground. Sources with positions known from low-frequency radio surveys were projected out of the data; the brightest sources were also measured at 31 GHz with the Owens Valley Radio Observatory (OVRO) 40 m telescope and subtracted directly from the data. The OVRO data allowed a complementary treatment of this potentially limiting population, giving us great confidence in our bright source treatment. We estimated the power level due to sources too faint to appear in the low-frequency radio source catalogs from 30 GHz number counts determined from CBI and OVRO data. The contribution of these residual sources is 114 μK^2, a factor of 4.5 below the observed excess, and we estimated an uncertainty of $\sim$57 μK^2 in this contribution. The reader can find further discussion of both the CBI deep field spectrum and the treatment of the radio source foreground in Paper II.

Although the significance of the excess power is not conclusive, it provides tantalizing evidence for the presence of secondary contributions to the microwave background anisotropies. One of the strongest expected secondary signals is the signature of the scattering of CMB photons by hot electrons in clusters, known as the Sunyaev-Zel'dovich (SZ) effect (Sunyaev & Zel'dovich 1970). The scattering leads to spectral distortions and anisotropies in the CMB. At the CBI observing frequencies the net effect is a decrement in the temperature along the line of sight. (However, as described in § 4, the lead minus trail differencing used in the CBI observations results in positive and negative SZ signals in equal measure, so this cannot be used as a discriminating signature in our data.) The SZ effect is expected to dominate over the primary anisotropies on scales of a few arcminutes.

In this paper we explore the possibility that the excess observed in the CBI deep fields may be a signature of the SZ effect. In § 2 we describe constraints on the normalization of the mass fluctuations σ_8 and shape parameter Γ from CMB experiments and a number of independent surveys. These parameters are critical in determining the amplitude of the SZ effect over the scales of interest to the CBI results. In § 3 we show the predicted power spectra for the SZ effect for various cosmological models. We use numerical methods to estimate the contribution from the SZ effect to the CMB power spectrum. In § 4 we use simulated CBI observations of SZ-contaminated CMB realizations to investigate the effect of an SZ foreground on our band power estimation methods. In § 5 we extend an image-filtering technique introduced in Paper IV to include specific template filters for the SZ effect. Our results and conclusions are discussed in § 6.

2. AMPLITUDE AND SHAPE PARAMETERS FOR LARGE-SCALE STRUCTURE FROM CMB DATA

The SZ power spectrum has a strong dependence on the amplitude of the density fluctuations. The amplitude is usually parameterized by the rms of the (linear) mass fluctuations inside 8 h^{-1} Mpc spheres, σ_8. We now summarize the constraints we can obtain on the amplitude and shape of the matter power spectrum from CMB data and compare them to results from weak-lensing surveys and cluster abundance data. Our parameter estimation pipeline also includes large-scale structure (LSS) priors that are designed to encompass the range in estimations from such experiments, as described below.

We use the parameter Γ to define the shape, following Bardeen et al. (1986, hereafter BBKS) and Efstathiou et al. (1992, hereafter EBW92). A by-product of linear perturbation calculations used to compute C_l in our database is transfer functions for density fluctuations, which can be related to LSS observables. Various (comoving) wavenumber scales determined by the transport of the many species of particles present in the universe characterize these spectra. The most important scale for dark matter–dominated universes is $k_{\rm Heq}^{-1}$, that of the horizon at redshift $\Omega_m/\Omega_{\rm er}$ when the density in nonrelativistic matter, $\Omega_m\bar{a}^{-3}$, equals that in relativistic matter, $\Omega_{\rm er}\bar{a}^{-4}$. This defines $\Gamma_{\rm eq}$: $k_{\rm Heq}^{-1} = 5\Gamma_{\rm eq}^{-1}\ h^{-1}$ Mpc, where $\Gamma_{\rm eq} = \Omega_m\ h\ [\Omega_{\rm er}/(1.68\Omega_\gamma)]^{-1/2}$. For the cases that we consider here, we simply have fixed the relativistic density to correspond to the photons and three species of very light neutrinos, so $\Gamma_{\rm eq} = \Omega_m\ h$.

Certain functional forms for the transfer functions are popular: In EBW92 a form was adopted that fitted a specific $\Omega_b = 0.03$ CDM model, but it is more general to adopt a fit to the $\Omega_b \to 0$ form given in BBKS, appropriately corrected for the difference between the temperature of the CMB estimated then and that known so well now (Bond 1996).[9] Although the coefficients of fits to detailed models vary with ω_b, h, and ω_m, which in particular result in oscillations in the transfer function for large ω_b/ω_m, it turns out that replacing $\Gamma_{\rm eq}$ by $\Gamma = \Gamma_{\rm eq}\exp(-\{\Omega_b[1+\Omega_m^{-1}(2h)^{1/2}]-0.06\})$ works reasonably well, to about 3% over the region most relevant to LSS (Sugiyama 1995; Bond 1996). Furthermore, as shown in Bond (1994), replacing Γ by $\Gamma_{\rm eff} = \Gamma + (n_s - 1)/2$ takes into account the main effect of spectral tilt over this LSS wavenumber band. It has also been shown that the Γ-models do fit the Automatic Plate Measuring (APM) Galaxy Survey and Two Degree Field Galaxy Redshift Survey (2dFGRS) data reasonably well at this stage. Particularly exciting is the prospect that the baryonic oscillations may be seen, but this is not required by the data yet. The approximate codification of a vast array of models in a single $\Gamma_{\rm eff}$ variable simplifies the treatment of LSS in the CMB data enormously.

The other variable we use to construct the LSS prior is the combination $\sigma_8\Omega_m^{0.56}$. Although various fits to cluster abundances give slightly different exponents than 0.56, this factor is consistent with a number of other measures, and we adopt this form as a representative value. These invariably involve the biasing factor b_g for the galaxies involved. For example, the expression relating the galaxy flow field to the galaxy density field inferred from redshift surveys takes the form $b_g\sigma_8\beta_g$, where $\beta_g = \Omega_m^{0.56}/b_g$ is a numerical factor whose value depends on the data set and analysis procedure. A combination such as this also enters into redshift space distortions. A great advantage of the weak-lensing and cluster abundance results shown in the figures is that they are independent of galaxy bias. However, for the cluster case, assumptions are needed, which, as the spread in estimates indicates, lead to uncertainties.

In Figures 1 and 2 we show the effect of the different priors on the distributions of σ_8 and $\sigma_8\Omega_m^{0.56}$, respectively. We also compare these to the weak-lensing results shown in the figures. The Red Cluster Survey results of Hoekstra et al. (2002) and the Virmos-Descart Survey results of van Waerbeke et al. (2002) correspond to a version of a weak prior: they marginalize over $\Gamma_{\rm eff}$ in the range 0.1–0.4, which is largely equivalent for this application to marginalization over ω_b, n_s, and ω_m. They also marginalize over the uncertainty in the mean redshift of the

[9] Available at http://www.cita.utoronto.ca/~bond/papers/houches/LesHouches96.ps.gz.

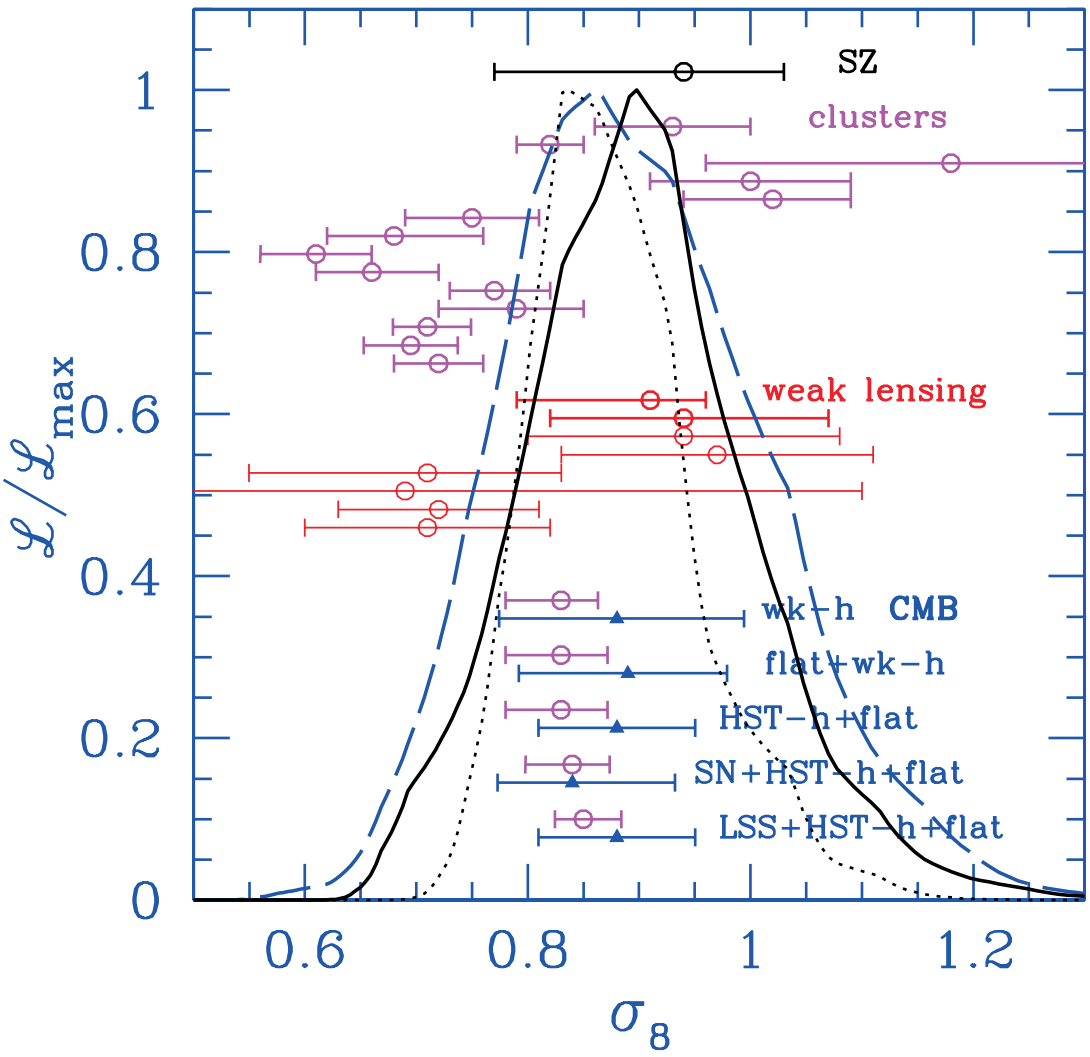

FIG. 1.—One-dimensional projected likelihood functions of σ_8 calculated for the CMB data with three prior probability restrictions on the cosmological parameters, contrasted with estimates from other data sets. The curves shown used the "all-data" set for the CMB as given in Paper V, namely, data from DMR, DASI (Halverson et al. 2002), BOOMERANG (for the Ruhl et al. [2003] cut), MAXIMA (Lee et al. 2001), the Very Small Array (VSA; Scott et al. 2003), and the CBI mosaic data for the odd $\Delta l = 140$ binning. The marginalization has been performed over seven cosmological variables and all of the relevant calibration and beam uncertainty variables associated with the experiments, seven in this case. Application of the weak-h prior is shown by the dashed blue curve, application of the flat weak-h prior is shown by the solid black curve, and application of the LSS flat weak-h prior is shown by the dotted black curve. Adding TOCO (Miller et al. 1999), the BOOMERANG test flight, and 17 other experiments predating 1999 April also gives very similar results. The Bayesian 50% and associated 16% and 84% error bars are shown as data points in blue for these and other priors, in particular those with the stronger *HST* measurement of h included and with SN data included. The purple data points with smaller errors are those determined with the all-data set to 2003 March, including *WMAP* data, as described in Bond et al. (2003). The original LSS prior was constructed on the basis of the cluster abundance data (Bond 1996; Bond & Jaffe 1999; Lange et al. 2001). An SZ estimate of σ_8 from Goldstein et al. (2003) that simultaneously determines amplitudes for a best-fit primordial spectrum and an SZ spectrum for our CBI deep field data in conjunction with ACBAR (Kuo et al. 2004) and BIMA (Dawson et al. 2002) data is shown at the top. Estimates of σ_8 from cluster abundance data and from weak-lensing data are also shown. These results have invariably had more restrictive priors imposed than those for the CMB and so are not always applicable, but the overall level of agreement in the various approaches is encouraging. From top to bottom, the sample cluster values are from Eke et al. (1996), Carlberg et al. (1997), Bahcall & Fan (1998), Pen (1998c), Pierpaoli et al. (2001), Reiprich & Böhringer (2002), Seljak (2002), Viana et al. (2002), Borgani et al. (2001), then two estimates from Pierpaoli et al. (2003), then from Schuecker et al. (2003), Allen et al. (2003), and Voevodkin & Vikhlinin (2004). From top to bottom, the weak-lensing estimates are from Hoekstra et al. (2002), van Waerbeke et al. (2002), Refregier et al. (2002), Bacon et al. (2003), Jarvis et al. (2003), Hamana et al. (2003), Brown et al. (2003), and Heymans et al. (2004).

lensed galaxies z_s, from 0.27 to 0.34 in the former case and 0.78 to 1.08 in the latter case. On the other hand, the cosmology was kept fixed with $\Omega_m = 0.3$. Refregier et al. (2002) and Bacon et al. (2003) adopt a more restrictive parameter range. If the weak marginalization schemes of Hoekstra et al. (2002) and van Waerbeke et al. (2002) were used, the error bars would increase in these cases. (Recently van Waerbeke et al. [2005] have improved the Virmos-Descart Survey analysis, which lowers the van Waerbeke et al. [2002] σ_8 estimate by 12%.) Figures 1 and 2 show sample cluster abundance estimates of σ_8 that are discussed below.

Van Waerbeke et al. (2002) give a weak-lensing result of $\Gamma_{\rm eff} = 0.25 \pm 0.13$ with marginalization over Ω_m from 0.1 to 0.4 and over σ_8. This is not explicitly shown in Figure 3, where we plot the prior probability we adopted for $\Gamma_{\rm eff}$. The APM result is the long-standing one used to construct the original prior, in which $\Gamma_{\rm eff}$ in the 0.15–0.3 range provided a good fit to the data, e.g., EBW92 and Bond (1996). Recent 2dFGRS (Peacock et al. 2001) and Sloan Digital Sky Survey (SDSS; Szalay et al. 2003) results shown give compatible results. Dodelson et al. (2002) estimate $0.14^{+0.11}_{-0.06}$, with errors at 95% confidence, for SDSS. Szalay et al. (2003) also give an estimate of σ_8 of 0.92 ± 0.06, but the

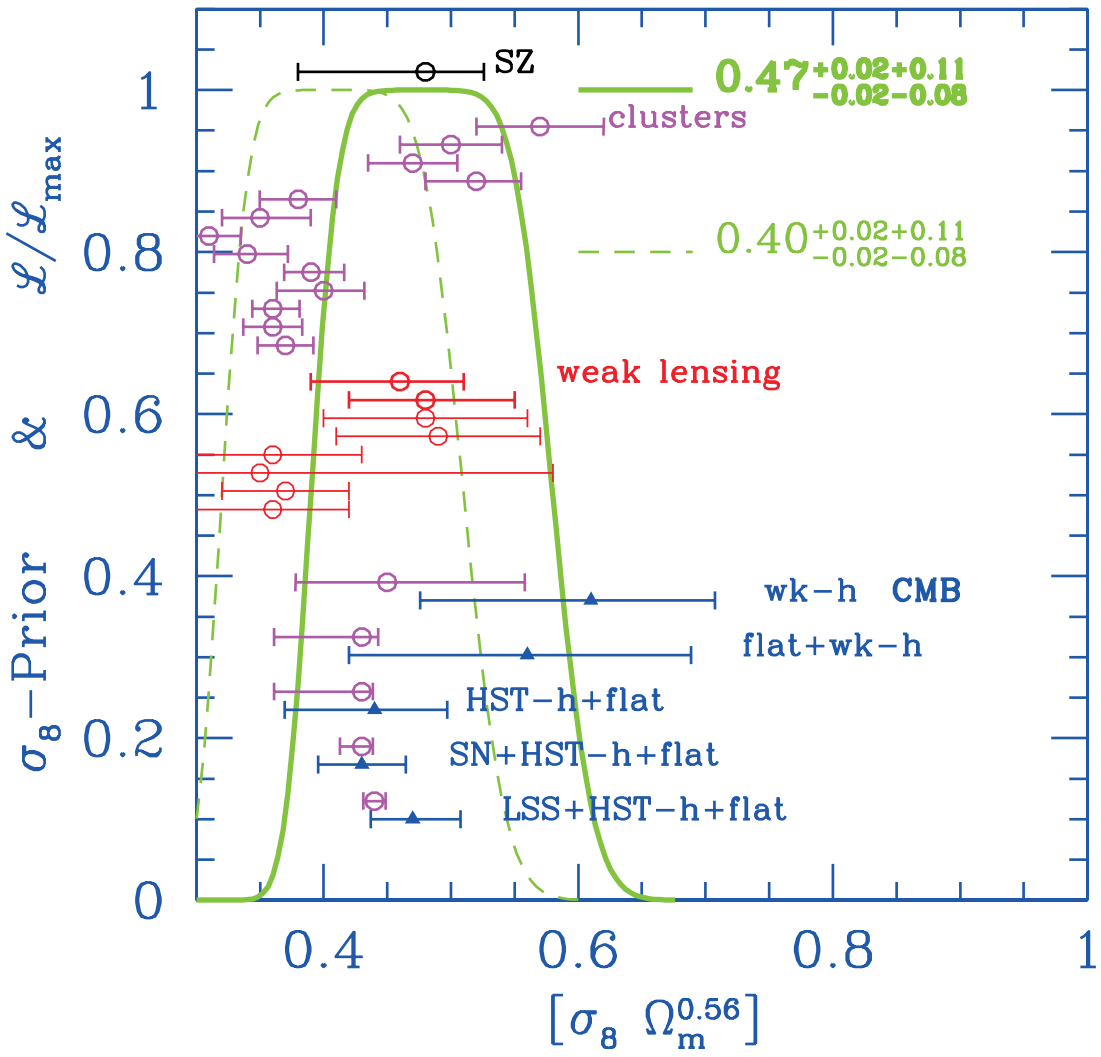

FIG. 2.—Weak prior used for LSS in $\sigma_8\Omega_m^{0.56}$, compared with estimates from SZ, cluster abundances, weak lensing, and the CMB data shown in Fig. 1, appropriately scaled. The blue error bars are for the all-data set to 2002 June, and the purple error bars are for the all-data set to 2003 March. The prior used in past work was shifted up in central value from 0.47 to 0.55 but is otherwise the same. We have also considered the LSS(low-σ_8) case (*dashed green curve*), with the prior shifted downward to be centered on 0.40 to accommodate better the low cluster abundance estimates, with results shown in Tables 1 and 2.

issue of galaxy biasing is folded into this determination. Although there are indications from the 2dF survey that biasing for the relevant galaxies is nearly unity from redshift-space distortions ($b = 1.04 \pm 0.11$; Verde et al. 2002) and the result is therefore compatible with the results shown, such results are not as directly applicable as those from clusters and from lensing, which directly relate to matter density power spectrum amplitudes.

The LSS prior used here and in Paper V involves a combination of constraints on the amplitude parameter $\sigma_8\Omega_m^{0.56}$ and on the shape parameter $\Gamma_{\rm eff}$. It differs slightly from that used in Lange et al. (2001), Jaffe et al. (2001), and Netterfield et al. (2002). We use $\sigma_8\Omega_m^{0.56} = 0.47^{+0.02,+0.11}_{-0.02,-0.08}$, distributed as a Gaussian (first error) smeared by a uniform (top hat) distribution (second error). We constrain the shape of the power spectrum via $\Gamma_{\rm eff} \equiv \Gamma + (n_s - 1)/2 = 0.21^{+0.03,+0.08}_{-0.03,-0.08}$, where $\Gamma \approx \Omega_m\, h\, e^{-\{\Omega_B[1+\Omega_m^{-1}(2h)^{1/2}]-0.06\}}$. In earlier work a central value of $\sigma_8\Omega_m^{0.56} = 0.55$ was used, together with $\Gamma_{\rm eff} = 0.22^{+0.07,+0.08}_{-0.04,-0.07}$. The old Γ prior is compared with the current version in Figure 3. The change does not affect the parameter values obtained.

The original σ_8 prior choice was motivated by fits to the cluster temperature distribution, as was the decision to lower the central value by 15% that has been made here. Our philosophy is to make the distribution broad enough that reasonable uncertainties are allowed for in the prior. For example, there are many models that do not fit the shape as well as the amplitude of the cluster distribution function. Thus, the best σ_8 for a given model depends on the temperature range chosen for the fit, and other physics might be involved. Especially with the reduced model spaces often considered, the formal statistical errors can look spectacularly good, but systematic issues undoubtedly dominate. Curiously, with the 15% drop, it appears that the σ_8 prior chosen could have been designed for the (weak) results from weak lensing. We test sensitivity by showing results for an "LSS(low-σ_8)" prior that has a further drop of 15%: $\sigma_8\Omega_m^{0.56} = 0.40^{+0.02,+0.11}_{-0.02,-0.08}$. This also accommodates some of the recent lower σ_8 estimates from cluster abundances, many of which use the X-ray luminosity as an indicator of mass, calibrated by observations. (We note that the reanalyzed Virmos-Descart Survey result [van Waerbeke et al. 2005] gives $\sigma_8\Omega_m^{0.56} = 0.43 \pm 0.04$, similar to the value obtained from the CMB-only data when *WMAP* data are included.)

We discuss the simulations in detail below, but we note here that the cases that we have run simulations on have $\sigma_8 = 0.9$ and 1.0 and $\Gamma_{\rm eff} = 0.18$ and 0.21. The detailed baryonic dependence of the transfer function was included in the 0.18 case.

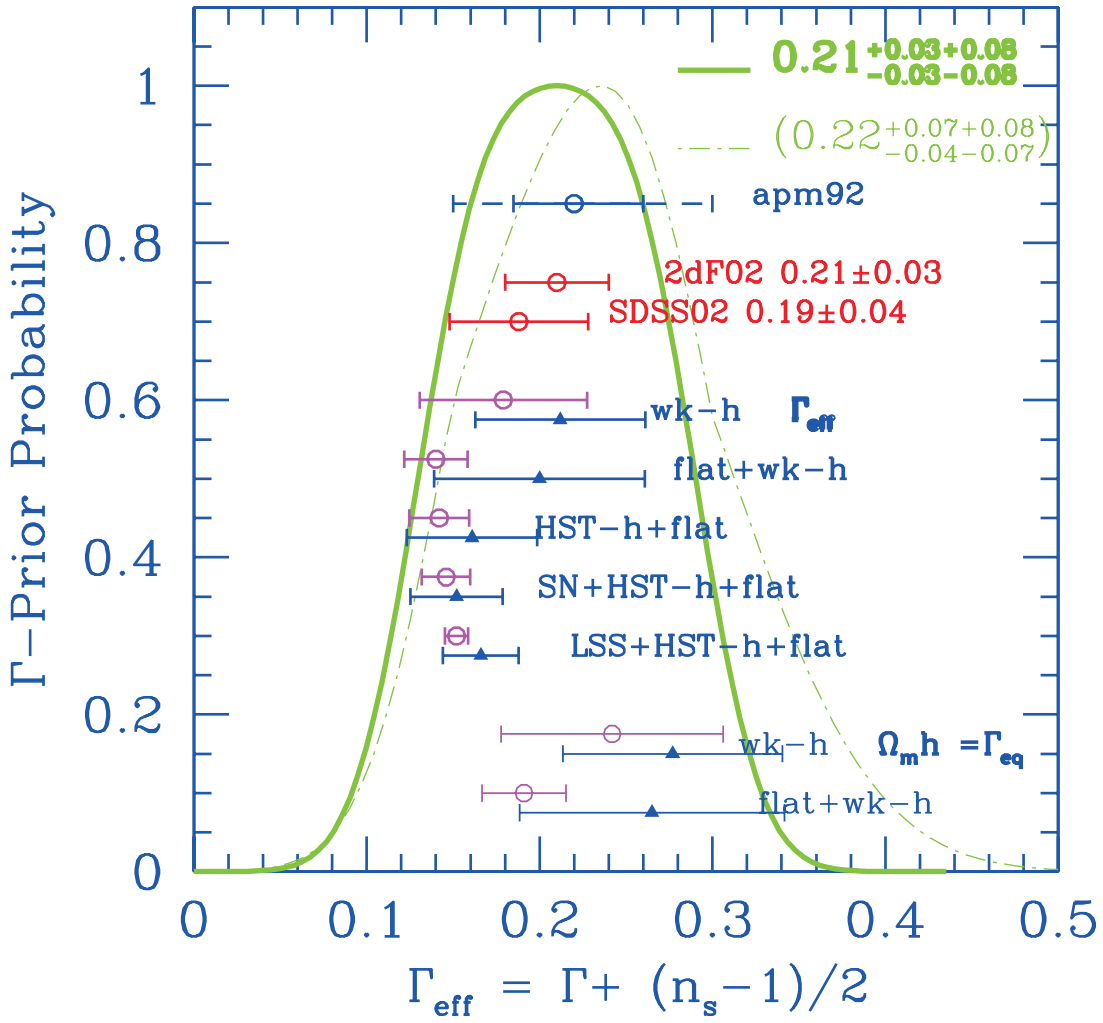

FIG. 3.—Prior probability used for the shape parameter $\Gamma_{\rm eff}$ (*solid green curve*). (This is to be contrasted with the more skewed one used in Lange et al. [2001], etc.; *light dash-dotted green curve*.) The Γ-prior was designed to encompass the range indicated by the APM data, vintage 1992, but estimates from the 2dFGRS and SDSS shown below are quite compatible. The CMB results for $\Gamma_{\rm eff}$ are shown with various choices for priors for comparison. Solid blue triangles with errors are for the all-data set as of 2002 June, as described in Paper V, and purple circles with errors are for the data as of 2003 March, as described in Bond et al. (2003). Here $\Gamma_{\rm eff}$ includes corrections for ω_b, h, and the tilt. The related values of $\Omega_m h$ are shown at the bottom to show the effect of these corrections.

The parameter choices were $\omega_b = 0.022$ and 0.0245, $h = 0.7$, and $\Omega_m = 0.3$ and 0.37. A best-fit model to the data for many prior choices has $\omega_b = 0.0225$, $\omega_c = 0.12$, $n_s = 0.95$, $\tau_C = 0.1$, $\Omega_\Lambda = 0.7$, $h = 0.69$, $\Omega_b = 0.047$, and $\Omega_{\rm cdm} = 0.253$, with a 13.7 Gyr age; the normalization is $\sigma_8 = 0.84$ and $\Gamma = 0.17$, with $\Gamma_{\rm eff} = 0.15$.

In general, CMB data provide weak constraints on the normalization of the matter fluctuations due to the added effects of the spectral tilt n_s and the optical depth parameter τ_C on the overall amplitude of the CMB power spectrum. Allowing for tensor modes in the power spectrum introduces further degeneracies. As shown in Paper V, when fitting for a given parameter we adopt the conservative and more computationally intensive approach of marginalizing over all other variables considered.

In Table 1 we summarize the constraints on the LSS parameters from the CMB data used in Paper V and a combination of priors. The mean and quoted (1 σ) errors correspond to the 50%, 16%, and 84% integrals of the marginalized likelihoods, respectively.

In Figures 4 and 5 we show the correlation of σ_8 with other parameters considered. Correlations with τ_C are nontrivial, and allowing the space to be open in τ_C does tend to give higher marginalized σ_8. The CMB data as of 2002 June did not give an indication of a τ_C detection, and we have imposed no physical prior on those results.

The addition of the first-year *WMAP* data and other data that have appeared since sharpens the determination of the parameters σ_8, $\sigma_8\Omega_m^{0.56}$, and $\Gamma_{\rm eff}$. This 2003 March compilation of CMB anisotropy data, described in Bond et al. (2003), is treated in the same way as the 2002 June data are in Paper V, with the same C_l-database. Results are shown in Table 2 and in the reduced errors in Figures 1, 2, and 3. For the 2003 March data, a prior was included on τ_C to accommodate the $\tau_C = 0.16 \pm 0.04$ detection reported by the *WMAP* team (Kogut et al. 2003). The form we have adopted has a top-hat spread convolved with a Gaussian distribution, as for our $\sigma_8\Omega_m^{0.56}$ and $\Gamma_{\rm eff}$ priors: $\tau_C = 0.16^{+0.04,+0.06}_{+0.04,+0.06}$. Similar results are obtained using the Markov chain Monte Carlo approach, which explicitly includes the τ_C-detection using the "TE" data of Kogut et al. (2003).

Best-fit models may have lower σ_8 values than the marginalized values. Typical best-fit models for the 2002 June data set are $\Omega_{\rm cdm} = 0.47$, $\Omega_\Lambda = 0.50$, $\Omega_b = 0.079$, $h = 0.51$, $n_s = 0.90$, $\tau_C = 0$, and $\sigma_8 = 0.72$ for the weak prior case and $\Omega_{\rm cdm} = 0.44$, $\Omega_\Lambda = 0.50$, $\Omega_b = 0.063$, $h = 0.57$, $n_s = 0.90$, $\tau_C = 0$,

TABLE 1

AMPLITUDE AND SHAPE PARAMETERS FOR LSS FROM THE CMB: SET OF ''ALL-DATA,'' 2002 JUNE COMPILATION

Priors	σ_8	$\sigma_8\Omega_m^{0.56}$	$\Gamma_{\rm eq}$	Γ	$\Gamma_{\rm eff}$
Weak-h	$0.88^{+0.13}_{-0.12}$	$0.61^{+0.16}_{-0.22}$	0.28 ± 0.07	0.23 ± 0.06	0.21 ± 0.05
Weak-h+LSS	$0.83^{+0.11}_{-0.10}$	$0.52^{+0.06}_{-0.11}$	0.23 ± 0.04	0.20 ± 0.04	0.18 ± 0.03
Weak-h+LSS(low-σ_8)	0.81 ± 0.10	$0.45^{+0.06}_{-0.08}$	0.21 ± 0.04	0.17 ± 0.04	0.17 ± 0.03
Weak-h+SN	$0.85^{+0.15}_{-0.12}$	$0.45^{+0.11}_{-0.08}$	0.21 ± 0.03	0.17 ± 0.03	0.17 ± 0.03
Flat+weak-h	$0.89^{+0.10}_{-0.11}$	$0.56^{+0.23}_{-0.25}$	0.26 ± 0.08	0.23 ± 0.08	0.20 ± 0.07
Flat+weak-h+LSS	$0.87^{+0.08}_{-0.07}$	$0.50^{+0.07}_{-0.11}$	0.23 ± 0.04	0.20 ± 0.04	0.17 ± 0.03
Flat+weak-h+LSS(low-σ_8)	$0.84^{+0.09}_{-0.08}$	$0.43^{+0.06}_{-0.09}$	0.20 ± 0.04	0.17 ± 0.03	0.15 ± 0.03
Flat+weak-h+SN	$0.85^{+0.11}_{-0.09}$	$0.43^{+0.10}_{-0.11}$	0.20 ± 0.03	0.17 ± 0.03	0.15 ± 0.03
Flat+*HST*-h	0.86 ± 0.11	$0.44^{+0.13}_{-0.16}$	0.21 ± 0.05	0.18 ± 0.05	0.16 ± 0.04
Flat+*HST*-h+LSS	0.88 ± 0.08	$0.47^{+0.08}_{-0.07}$	0.22 ± 0.03	0.19 ± 0.03	0.17 ± 0.03
Flat+*HST*-h+SN	$0.84^{+0.11}_{-0.08}$	0.43 ± 0.08	0.20 ± 0.03	0.17 ± 0.03	0.15 ± 0.03
Flat+*HST*-h+LSS+SN	$0.87^{+0.09}_{-0.08}$	$0.45^{+0.07}_{-0.05}$	0.21 ± 0.02	0.18 ± 0.02	0.16 ± 0.03
Flat+*HST*-h+LSS(low-σ_8)+SN	$0.85^{+0.09}_{-0.07}$	0.43 ± 0.05	0.20 ± 0.02	0.17 ± 0.02	0.15 ± 0.02

NOTES.—Amplitude and shape parameter estimates from various data sets, for various prior probability choices and using the set of ''all-data'' for the CMB as described in Paper V, in particular DMR, DASI, MAXIMA, BOOMERANG (Ruhl et al. [2003] cut), VSA, and CBI mosaic data for the odd $\Delta l = 140$ binning, as described in Paper III. In the first four rows, the weak prior in h ($0.45 < h < 0.90$) is imposed (including further weak constraints on cosmological age, $t_0 > 10$ Gyr, and matter density, $\Omega_m > 0.1$). The sequence shows what happens when priors for LSS (with $\sigma_8\Omega_m^{0.56}$ centered about 0.47), for LSS(low-σ_8) (with the σ_8 distribution shifted downward by 15%, centered about 0.40), and for SN are imposed. While the first four rows allow $\Omega_{\rm tot}$ to be free, the next four have $\Omega_{\rm tot}$ pegged to unity, a number strongly suggested by the CMB data. The final five rows show the ''strong-h'' prior, a Gaussian centered on $h = 0.71$ with dispersion ± 0.07, obtained for the Hubble key project. The $t_0 > 10$ Gyr and $\Omega_m > 0.1$ constraints are also imposed, but they have no impact. Central values and 1 σ limits for the seven database parameters that form our fiducial minimal inflation model set are found from the 16%, 50%, and 84% integrals of the marginalized likelihood for σ_8 and $\sigma_8\Omega_m^{0.56}$. For $\Gamma_{\rm eq} \equiv \Omega_m h$, Γ, and $\Gamma_{\rm eff}$, the values are means and variances of the variables calculated over the full probability distribution. Shifting the center of the $\sigma_8\Omega_m^{0.56}$ prior downward by 15% to accommodate more of the low cluster results has little effect on the flat+*HST*-h+LSS+SN result.

and $\sigma_8 = 0.81$ for flat+weak and flat+weak+LSS priors. These σ_8 values are lower because the best fits selected the $\tau_C = 0$ peak in the likelihood, whereas integration over the relatively broad τ_C likelihood allows for the inclusion of high-σ_8 models. If the *Hubble Space Telescope* (*HST*-h) or supernova (SN) prior is included along with LSS, the best-fit model is a more conventional ΛCDM one, with $\tau_C = 0.1$: $\Omega_{\rm cdm} = 0.25$, $\Omega_\Lambda = 0.70$, $\Omega_b = 0.047$, $h = 0.69$, $n_s = 0.95$, $\tau_C = 0.1$, and $\sigma_8 = 0.84$. For the 2003 March data with the τ_C prior, this $\tau_C = 0.1$ model also provides a best fit for the weak+flat and weak+flat+LSS cases.

Comparison of our results with independent estimates of σ_8 from CMB data is complicated by the different choices of parameter marginalization and by different treatments of the CMB data. Lahav et al. (2002) carried out a joint CMB-2dFGRS analysis of cosmological parameters. Their result is $\sigma_8 = 0.73 \pm 0.05$ after marginalizing over some variables but keeping τ_C fixed at 0 and n_s fixed at unity. This value is therefore biased low with respect to nonzero τ_C models. They also show how letting τ_C vary gives higher values for σ_8. Melchiorri & Silk (2002) quote smaller values for σ_8 in their analysis, even when τ_C was allowed to vary.

The values we obtain for the 2003 March data set are in good agreement with those obtained by the *WMAP* team (Spergel et al. 2003). However, we caution that the projected distribution of σ_8 from the CMB depends on the other parameters. For the seven-parameter inflation-motivated models considered here, there is a strong correlation of σ_8 with the Thomson scattering depth τ_C and the primordial spectral index n_s. If, in addition, n_s is allowed a logarithmic correction with wavenumber, introducing another parameter highly correlated with σ_8, the distribution extends to higher σ_8 (Bond et al. 2003). Allowing for a gravity wave contribution extends the distribution to lower σ_8. These caveats about the effect of adding extra parameters in the CMB analysis, together with the scatter in the estimates of σ_8 from clusters and weak lensing shown in Figures 1 and 2, reflect the current uncertainty as to whether a low or high σ_8 will emerge.

3. THE ANGULAR POWER SPECTRUM OF THE SUNYAEV-ZEL'DOVICH EFFECT

The SZ effect is a signature of the scattering of CMB photons off hot electrons. The effect can be described in terms of the fractional energy gain per scatter along the line of sight. By multiplying by the number density of electrons and integrating along the line of sight, we can derive the induced temperature change:

$$\frac{\Delta T_{\rm SZ}}{T_{\rm CMB}} = -2y\psi_K(x) = -2\sigma_{\rm T}\int n_e \frac{k_{\rm B}(T_e - T_{\rm CMB})}{m_e c^2} d\chi\, \psi_K(x), \quad (1)$$

where y is the Compton y-parameter, $\sigma_{\rm T}$ is the Thomson cross section, n_e is the electron number density, T_e is the electron temperature, $T_{\rm CMB}$ is the CMB temperature, $k_{\rm B}$ is Boltzmann's constant, and $m_e c^2$ is the electron's rest mass energy. Here $\psi_K(x)$, with $x \equiv h\nu/k_{\rm B}T_{\rm CMB}$, is a frequency-dependent function that is unity at Rayleigh-Jeans wavelengths and is 0.975 at the 30 GHz frequencies probed by the CBI.

With the great increase in experimental sensitivity, measurement of the SZ effect in known clusters has become almost routine (see, e.g., Birkinshaw et al. 1984; Carlstrom et al. 1996; Holzapfel et al. 1997; Mason et al. 2001; Udomprasert et al. 2004; Grainge et al. 2002). Coupled with X-ray observations of the cluster, these measurements yield independent constraints on the value of the Hubble constant. They also provide a direct measurement of the amount of baryon mass in the cluster gas. The SZ effect is expected to contribute significantly to the CMB power spectrum at scales $l > 2000$, with a crossover point between the primary CMB and SZ signature occurring somewhere between $l \sim 2000$ and $l \sim 3000$. Surveys observing at these scales therefore require accurate component separation to reconstruct the primary CMB spectrum, and much work has focused on this issue in recent years. Many proposed experiments will

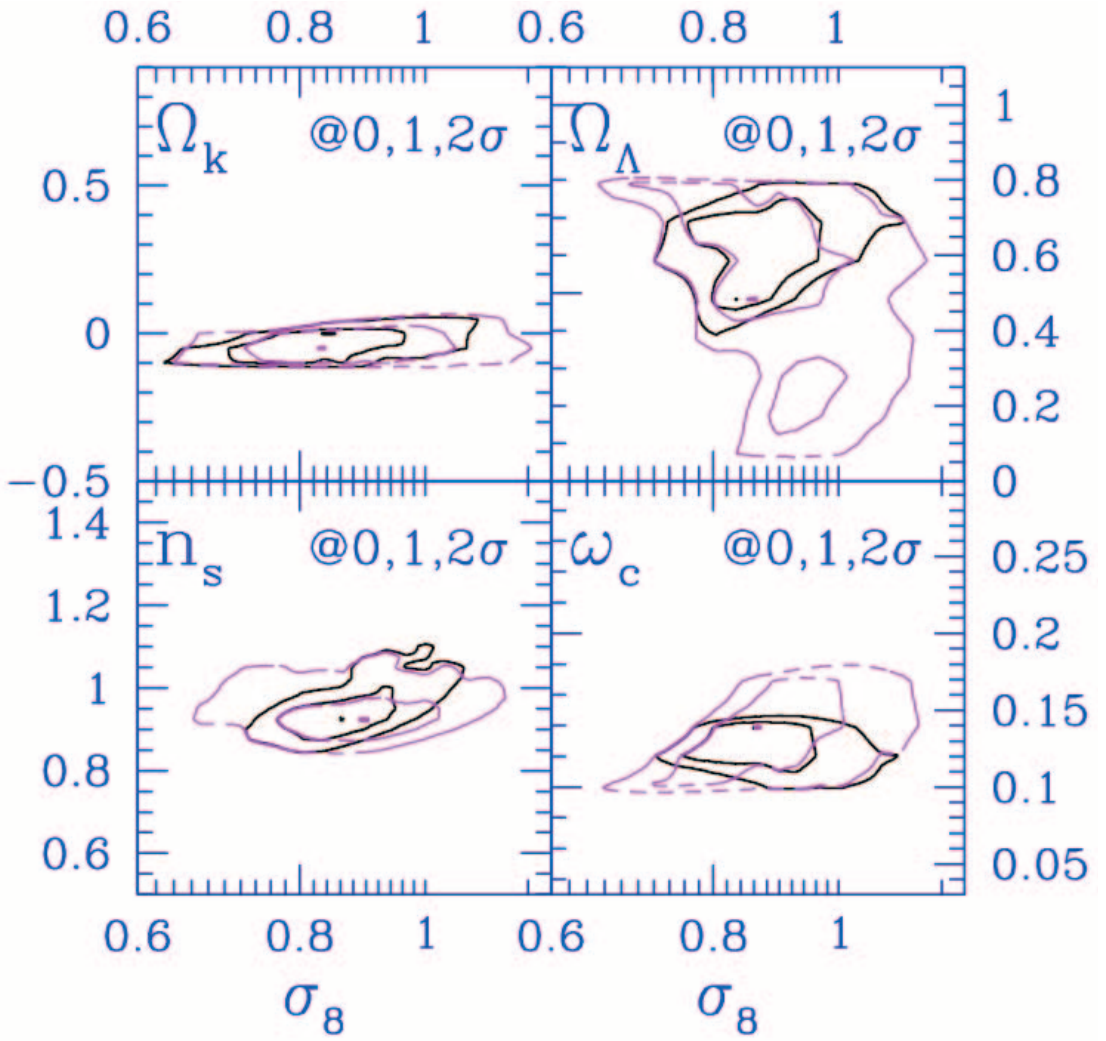

FIG. 4.—Contours of 1 and 2 σ for two-dimensional projected likelihood functions for various cosmological parameters vs. σ_8. For this case, the all-data set from the 2002 June compilation was used: DASI, MAXIMA, BOOMERANG, VSA, and the CBI mosaic data for the odd $\Delta l = 140$ binning. The Ω_k-σ_8 plot shows the weak-h prior (*purple*) and the LSS+weak-h prior (*solid black*). For the other three plots, the flat constraint was added to these two priors as well. Note the positive correlation with n_s but little correlation in the other variables.

adopt multifrequency observing strategies in order to separate the different components by their different spectral dependences. These techniques cannot be applied to the narrow frequency band of the CBI observations. However, we can attempt to address the question of whether the SZ effect could provide a contribution with the required amplitude to explain the observed excess.

We use the output of two separate hydrodynamic simulation algorithms in an attempt to predict the level at which the SZ effect contributes to the CBI deep field observations. We also relate our numerical results to analytical models of the SZ power spectrum based on the halo model.

3.1. *Hydrodynamic Simulations of the Sunyaev-Zel'dovich Effect*

The two codes that we have employed both provide high-resolution dark matter and hydrodynamic simulations of large-scale cosmic structure, which we use to generate simulated wide-field SZ maps. The simulation algorithms and processing techniques were developed independently (Pen 1998a; Bond et al. 1998, 2002; Wadsley et al. 2003) and are based on two different numerical schemes for solving the self-gravitating, hydrodynamic equations of motion. High-resolution gasdynamical simulations of large enough volumes are still beyond current technological capabilities. Following an approach taken previously by other authors (e.g., Springel et al. 2001), we create a pseudorealization of the cosmic structure up to high redshifts from a single, medium-sized, high-resolution simulation by stacking randomly translated and rotated (or flipped) copies of the (evolving) periodic volume.

One set of SZ simulations was obtained using the GASOLINE code, an efficient implementation of the (Lagrangian) smooth particle hydrodynamics (SPH) method (Wadsley et al. 2003). This tree+SPH code uses a pure tree-based gravity solver and has spatially adaptive time stepping. It has been parallelized on many architectures (MPI [Message Passing Interface] in this case) and shows excellent scalability. The results presented here are based on the analysis of three high-resolution ΛCDM simulations: two 200 Mpc box computations, with 256^3 dark matter particles plus 256^3 gas particles, and one 400 Mpc box computation, with 512^3 dark matter particles and 512^3 gas particles, a very large number for SPH simulations. The calculations were adiabatic, in the sense that only shocks could inject entropy into the medium. Despite the different sizes, all three simulations were therefore run with the same mass resolution. All simulations

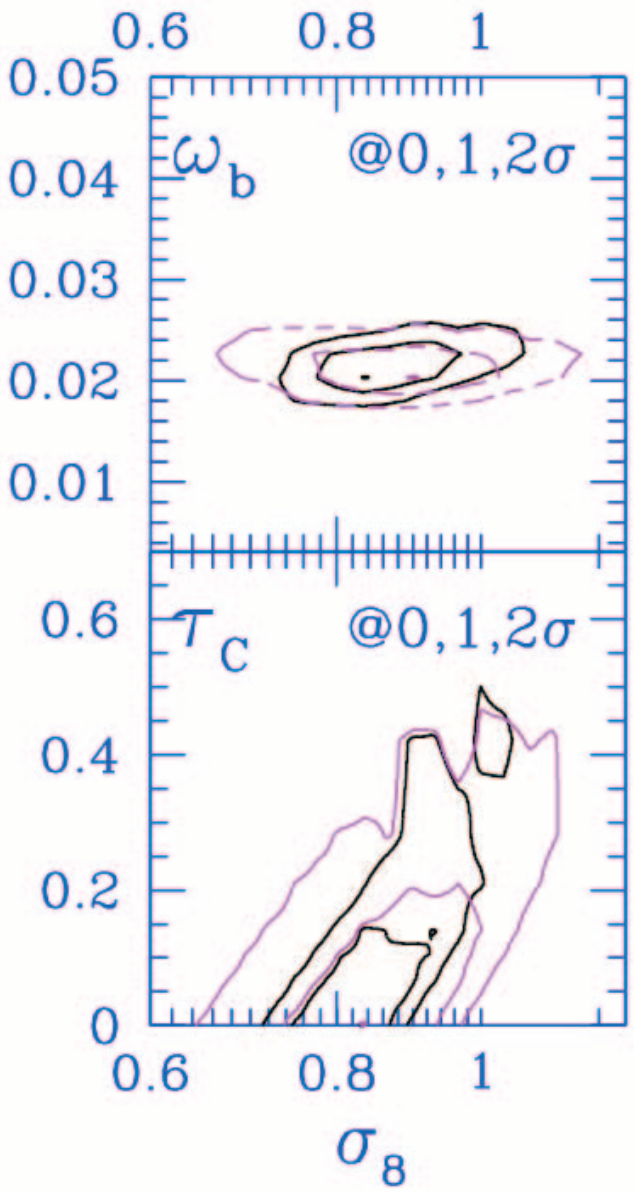

FIG. 5.—Contours of 1 and 2 σ for two-dimensional projected likelihood functions for ω_b and τ_C for the all-data set of Paper V. The flat+weak-h prior (*purple*) and flat+LSS+weak-h prior (*solid black*) cases are shown. The significant σ_8-τ_C correlation is evident, which results in a higher σ_8 for higher τ_C. One could impose a stronger prior than $\tau_C < 0.7$ (as is done here) on the basis of astrophysical arguments. This is fraught with uncertainty, since it involves the first objects collapsing on small scales in the universe and their efficiency in generating stars that produce ionizing radiation. However, τ_C has apparently been detected by *WMAP* at the 0.16 ± 0.04 level (Kogut et al. 2003), and results with a prior encompassing this detection on the 2003 March compilation of the data are given in Table 2.

were run with a gravitational softening of 50 kpc (physical). The scale probed by the SPH smoothing kernel was not allowed to become smaller than the gravitational softening in the 200 Mpc runs, but it was not limited in the 400 Mpc run, which attained gas resolution scales as low as 5 kpc in the highest density environments, although increasing considerably at lower density. (In the 400 Mpc run, 64 neighbors were required to be within the smoothing kernel.) The 512^3 simulation was performed on a large-memory, 114 (667 MHz) processor SHARCNET COMPAQ SC cluster at McMaster University. It required about 80 GB of memory and took ~40 days of wall time to run.

Another set of SZ maps was obtained using a 512^3 run of the moving mesh hydrodynamics (MMH) code of Pen (1998a). This code features a full curvilinear total variation diminishing (TVD) hydrodynamics code with a curvilinear particle mesh (PM) N-body code on a moving coordinate system. We follow the mass field such that the mass per unit grid cell remains approximately constant. This gives all the dynamic range advantages of SPH simulations combined with the speed and high resolution of grid algorithms. The box size was 143 Mpc, and the smallest grid spacing was 57 kpc (comoving). This 512^3 simulation used 30 GB of memory and took about three weeks (~1500 steps) on a 32 processor shared-memory Alpha GS320 using Open MP parallelization directives. The calculations were adiabatic as well.

The simulation boxes yield a number of projections of the gas distributions in random orientations and directions. The projections are then stacked to create a redshift range appropriate for the SZ simulation. In the case of the MMH simulation the angular size of the simulated box above a redshift of $z = 1.6$ is smaller than 2°, the required angular size of the SZ simulations. To include the contributions from higher redshifts, we tiled two copies of the periodic box to cover the increased angles. This only affects the smallest scales. All the maps were obtained with a low-redshift cutoff at $z = 0.2$ to minimize the contribution from the closest clusters in the projections. The computational costs of running such large hydrodynamic simulations prevented us from obtaining targeted simulations with identical cosmological parameters from both algorithms. Below we account for the parameter variations in the models run when comparing the two simulations, and we see a remarkable consistency between the results. The parameter variations are, in fact, an advantage for us, since they provide us with a sampling of the SZ effect amplitude for processing through the CBI pipeline. We summarize the parameters used in the simulations in Table 3.

The two 200 Mpc SPH simulations were used to generate 20 $2^\circ \times 2^\circ$ maps each, while the MMH simulation yielded 40 separate maps. A detailed analysis of the MMH maps including SZ statistics and non-Gaussianity is given by Zhang et al. (2002). A preliminary analysis of simulated SZ maps based on one of the 256^3 SPH simulations was presented by Bond et al. (2002), and a more detailed analysis of the 512^3 results will be presented elsewhere.

3.2. *Hydrodynamic Simulation Results*

In Figure 6 we show the results for the $\sigma_8 = 1.0$, 143 Mpc MMH simulation, the $\sigma_8 = 1.0$ and 0.9, 200 Mpc SPH simulations, and the $\sigma_8 = 1.0$, 400 Mpc SPH simulation. The curves show averages for the $\mathcal{C}_l = l(l+1)C_l/2\pi$ spectra from the 40 and 20 MMH and SPH maps, respectively. The shaded regions show the full excursion of the power spectra in each set of maps. This gives a partial indication of the scatter induced in the power because of the small areas being considered. We compare these with a best-fit model to the BOOMERANG, CBI, *COBE* Differential Microwave Radiometer (DMR), Degree Angular Scale Interferometer (DASI), and MAXIMA data and an optimal combination of the mosaic and deep CBI, BOOMERANG, *COBE* DMR, DASI, and MAXIMA band powers (Paper V). The combined spectrum is designed for optimal coverage with variable bandwidths over the range of scales considered. At scales above $l \sim 1000$, the optimal spectrum is dominated by the contributions of the CBI mosaic and deep results.

To compare the cosmological simulations, we have to account for the differences in parameters that the simulations were run with. The dominant effect for the SZ $\mathcal{C}_l$ spectrum is variation

TABLE 2
AMPLITUDE AND SHAPE PARAMETERS FOR LSS FROM THE CMB: SET OF ''ALL-DATA,'' 2003 MARCH COMPILATION

Priors	σ_8	$\sigma_8\Omega_m^{0.56}$	$\Gamma_{\rm eq}$	Γ	$\Gamma_{\rm eff}$
Weak-h	$0.83^{+0.04}_{-0.06}$	$0.45^{+0.24}_{-0.16}$	0.24 ± 0.07	0.20 ± 0.06	0.18 ± 0.05
Weak-h+LSS	$0.85^{+0.04}_{-0.03}$	0.44 ± 0.02	0.21 ± 0.02	0.17 ± 0.01	0.15 ± 0.02
Weak-h+LSS(low-σ_8)	0.84 ± 0.05	$0.43^{+0.02}_{-0.04}$	0.20 ± 0.02	0.17 ± 0.02	0.15 ± 0.02
Weak-h+SN	0.84 ± 0.05	$0.43^{+0.02}_{-0.13}$	0.20 ± 0.02	0.17 ± 0.02	0.14 ± 0.02
Flat+weak-h	$0.83^{+0.05}_{-0.06}$	$0.43^{+0.03}_{-0.16}$	0.19 ± 0.03	0.16 ± 0.03	0.14 ± 0.02
Flat+weak-h+LSS	$0.85^{+0.04}_{-0.03}$	0.44 ± 0.02	0.21 ± 0.01	0.17 ± 0.01	0.15 ± 0.01
Flat+weak-h+LSS(low-σ_8)	0.84 ± 0.05	$0.43^{+0.02}_{-0.04}$	0.20 ± 0.02	0.17 ± 0.02	0.15 ± 0.02
Flat+weak-h+SN	0.84 ± 0.05	$0.43^{+0.02}_{-0.13}$	0.20 ± 0.02	0.17 ± 0.02	0.14 ± 0.02
Flat+*HST*-h	$0.83^{+0.05}_{-0.06}$	$0.43^{+0.02}_{-0.16}$	0.19 ± 0.03	0.16 ± 0.03	0.14 ± 0.02
Flat+*HST*-h+LSS	$0.85^{+0.04}_{-0.03}$	0.44 ± 0.02	0.21 ± 0.01	0.17 ± 0.01	0.15 ± 0.01
Flat+*HST*-h+SN	$0.84^{+0.04}_{-0.05}$	$0.43^{+0.02}_{-0.04}$	0.20 ± 0.02	0.17 ± 0.02	0.15 ± 0.02
Flat+*HST*-h+LSS+SN	$0.85^{+0.04}_{-0.03}$	0.44 ± 0.02	0.21 ± 0.01	0.17 ± 0.01	0.15 ± 0.01
Flat+*HST*-h+LSS(low-σ_8)+SN	0.85 ± 0.04	$0.44^{+0.02}_{-0.03}$	0.20 ± 0.02	0.17 ± 0.02	0.15 ± 0.02

NOTES.—Similar to Table 1, but for an extension of the set ''all-data'' to include *WMAP*, ACBAR, extended VSA (Grainge et al. 2003), and CBI results, as well as DASI, BOOMERANG, and MAXIMA, analyzed in the same way. A further (weak) prior on τ_C was applied to accommodate the *WMAP* detection from the cross-correlation of temperature and polarization, but this makes little difference in the results. For example, without this extra prior, flat+weak-h shifts to 0.81 ± 0.05 and $0.41^{+0.03}_{-0.11}$. As in Table 1, the downshifted LSS prior has little effect on flat+*HST*-h+LSS+SN.

in σ_8 and $\Omega_b h$, scaling as σ_8^7 and $(\Omega_b h)^2$. Figure 6 (*top*) demonstrates that $\mathcal{C}_l \propto \sigma_8^7$ does indeed bring the 200 Mpc SPH run at $\sigma_8 = 0.9$ into essentially perfect alignment with the $\sigma_8 = 1$ run (*yellow points*). (Apart from the amplitude, the initial conditions in the simulations were otherwise the same.) The exact factor n in a scaling of the form $\mathcal{C}_l \sim (\Omega_b h)^2 \sigma_8^n$ depends on the model in question, but $6 \lesssim n \lesssim 9$ is typical (Zhang et al. 2002). Differences in Ω_m and the shape of the power spectrum also have an influence on $\mathcal{C}_l$, as Komatsu & Seljak (2002) discuss in more detail.

For the two separate σ_8 cases employed in the runs, we rescale the spectra to a nominal $\Omega_b h = 0.0314$, a value suggested by the CMB data. This enables us to compare the MMH result with the SPH results for the $\sigma_8 = 1$ runs (Fig. 6, *top*). We see that the two codes give similar amplitudes over the range considered, and, in particular, these are very similar over the scales of interest for the CBI deep field result (*green hatched box*). At larger angular scales, the MMH simulation shows a somewhat higher amplitude than the SPH simulation. This may be in part due to the presence of a large rare cluster in the MMH volume simulation. The Poisson noise contribution of the large cluster is aggravated by the resampling technique adopted in the SZ map-making stage described above. Variable redshift cutoffs do indeed confirm the dominant effect of this single cluster on the low-l tail of the spectrum.

At smaller angular scales the two results start to diverge. The differences in spectral shape and cosmological parameters should not account for this. It may be attributable to the different techniques used to limit the resolution that is achievable, but this needs more investigation.

In Figure 6 (*middle*) we have plotted the results from the 400 and 200 Mpc SPH simulations, which were both run with $\sigma_8 = 0.9$. We also compare this run to SZ power spectra derived from the 200 Mpc box SPH simulations of Springel et al. (2001). The cosmological parameters of the Springel et al. (2001) simulations were the same as those used in our SPH runs, except for a value of $\Omega_b h^2 = 0.018$. We also rescale this spectrum to the nominal $\Omega_b h = 0.0314$. The agreement is remarkable. We can contrast this level of agreement with the situation described in Springel et al. (2001), where it appeared that different codes were giving quite different results. Nonetheless, we plan a further exploration of the effects of lattice size variations and other numerical parameters to compare the MMH and SPH codes more exactly.

On the basis of these results, we can calibrate the expected power to compare with the wide-band result of Paper II:

$$\text{SPH}: \quad \mathcal{C}_l^{\rm SZ} \sim 170\ \mu\text{K}^2\, \frac{(\Omega_b h)^2}{0.0314^2}\, \sigma_8^7,$$

$$\text{MMH}: \quad \mathcal{C}_l^{\rm SZ} \sim 210\ \mu\text{K}^2\, \frac{(\Omega_b h)^2}{0.0314^2}\, \sigma_8^7. \qquad (2)$$

For $\sigma_8 = 1$ and $\Omega_b h = 0.0314$, these amplitudes are $\sim$0.4 relative to the noise level for the CBI joint analysis of the three deep fields.

3.3. *Analytic Modeling of the Sunyaev-Zel'dovich Power Spectrum*

The general analytic framework comes under the generic name of ''halo models,'' in which simple parameterized gas profiles within clusters and groups are constructed, appropriately scaled according to the masses. The gas profile in a halo and halo mass-temperature relation determines the SZ effect of the halo. The abundance of the halos as a function of mass and

TABLE 3
SIMULATION PARAMETERS

Code	Size (Mpc)	Resolution	σ_8	$\Omega_b h^2$	Ω_Λ	Ω_m	h	n_s	$\Gamma_{\rm eff}$
SPH	200	256^3	0.9	0.0200	0.70	0.30	0.70	1.0	0.18
SPH	200	256^3	1.0	0.0200	0.70	0.30	0.70	1.0	0.18
SPH	400	512^3	0.9	0.0220	0.70	0.30	0.70	1.0	0.18
MMH	143	512^3	1.0	0.0245	0.63	0.37	0.70	1.0	0.21

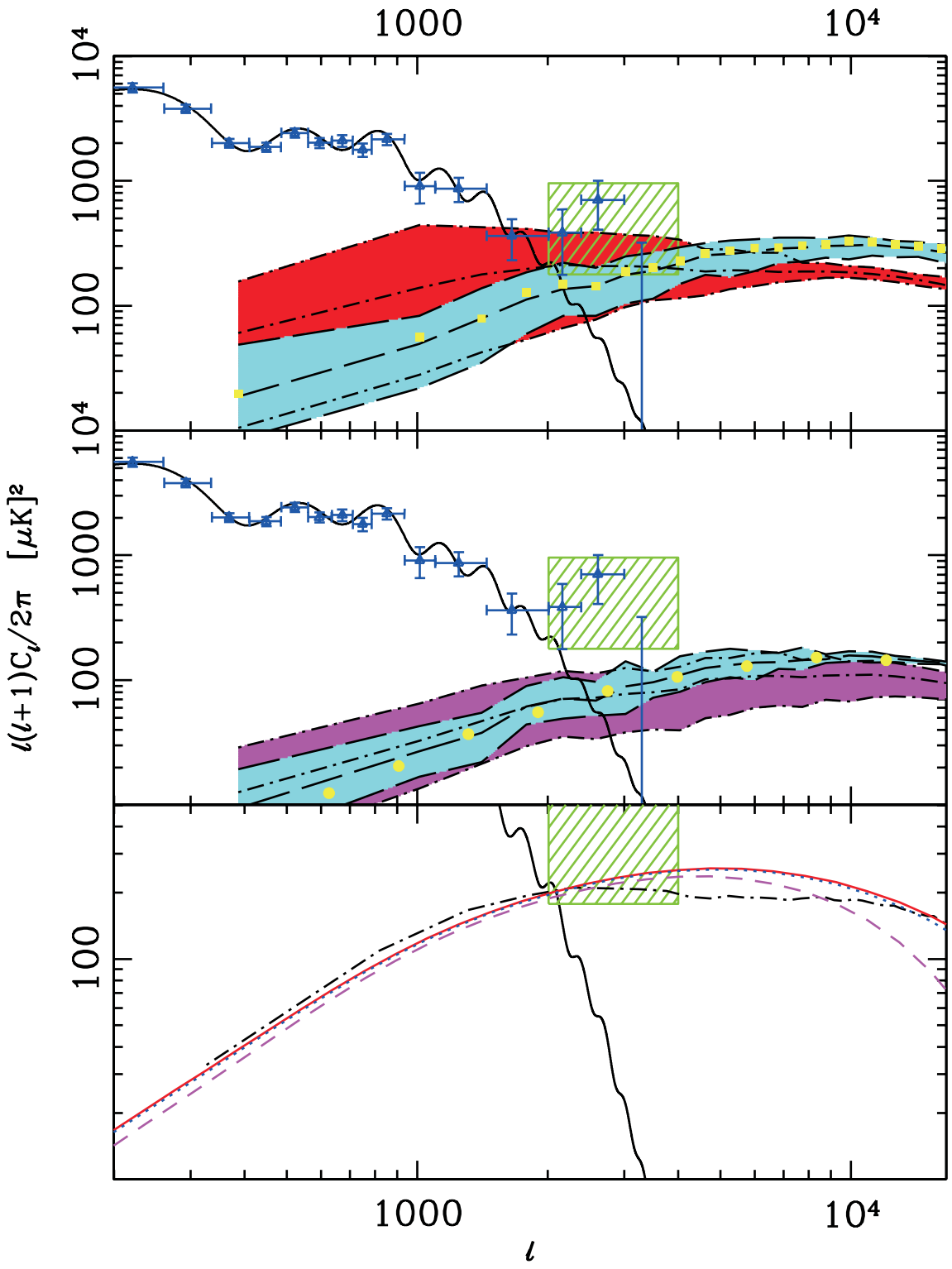

FIG. 6.—SZ power spectra for various simulations. All SZ spectra have been scaled to a common $\Omega_b h = 0.0314$, the best fit to the CMB data. The top panel shows the SZ spectra for the $\sigma_8 = 1.0$ SPH 256^3 200 Mpc (*cyan*) and MMH 512^3 140 Mpc (*red*) simulations. We also plot the power spectrum from the $\sigma_8 = 0.9$ SPH 256^3 200 Mpc run (*yellow points*), scaled using the relation of eq. (2). The target 2 σ region suggested by the deep data is shown as a green-hatched box. An optimal power spectrum combining all CBI data with the BOOMERANG, *COBE* DMR, DASI, and MAXIMA data is shown as blue triangles. The solid black curve is a best-fit model to the data out to $l = 2000$. The middle panel compares the $\sigma_8 = 0.9512^3$ 400 Mpc (*cyan*) and 256^3 200 Mpc (*purple*) SPH simulations. The yellow points are the spectra derived from the ΛCDM simulation of Springel et al. (2001), also scaled to $\Omega_b h = 0.0314$. The bottom panel compares the MMH results (*dot-dashed curve*) with the analytic halo model results described in § 3 for mass cuts of $0.001M_8$ (*solid red curve*), $0.01M_8$ (*dotted blue curve*), and $0.1M_8$ (*dashed purple curve*) described in the text. There is little sensitivity to a change in the lattice size over the l-range shown. We note that physical effects, such as early entropy injection, may change the effective mass cut.

redshift is determined by the Press & Schechter (1974) formula, the Bond & Myers (1996) peak-patch formula, or formulas derived from fits to *N*-body simulations. Clustering of the halos is included through simple linear biasing models. The halo model approach has been applied to the SZ effect by many authors over time (e.g., Bond 1988; Cole & Kaiser 1988; Makino & Suto 1993; Bond & Myers 1996; Atrio-Barandela & Mucket 1999; Komatsu & Kitayama 1999; Cooray 2000; Molnar & Birkinshaw 2000; Seljak et al. 2001). There has still not been an adequate calibration of the relation between the physical parameters describing the gas distribution in the halos and the results of gas-dynamical simulations, and usually the parameters that have been adopted are those derived from observations of clusters at low redshift. We show here that we can get reasonable fits to our simulation results by choosing suitable gas profile parameters. However, we caution that the gas profile is a function of halo mass and redshift, so global fitting to our simulated SZ power spectra may not deliver reliable parameters for the analytic model. For now, we take our globally fitted models to show sensitivity to parameter variations.

In Figure 6 (*bottom*), a few analytic models are compared with the $\sigma_8 = 1$ MMH simulation. The Press-Schechter distribution for the halo comoving number density n as a function of halo mass M and redshift z is

$$M\,dn/dM \propto (2/\pi)^{1/2}(\bar{\rho}_0/M)|d\ln\sigma/d\ln M|\nu e^{-\nu^2/2},$$

where $\nu \equiv \delta_c/\sigma$. Here $\bar{\rho}_0$ is the present mean matter density of the universe, and $\sigma(M, z)$ is the linear theory rms density fluctuation in a sphere containing mass M at redshift z. It is calculated using the input linear density power spectrum $P(k)$ of our simulations, which is truncated at $k_{\rm low} = 2\pi/L$ and $k_{\rm upp} = \sqrt{3}\pi N/L$ because of the finite box size L and resolution N of the simulations, respectively. In this formula, we have taken $\delta_c = 1.686$ as the linearly extrapolated spherical overdensity at which an object virializes. Although this is strictly valid only for $\Omega_m = 1$ cosmologies, when Ω_m decreases from 1 to 0.3, δ_c only decreases from 1.686 to $\sim$1.675 (Eke et al. 1996). We omit this dependence of δ_c on Ω_m, Ω_Λ, and therefore redshift for the $\Omega_m = 0.37$ ΛCDM we are trying to fit here. We also truncate the mass integral at a specified lower mass limit $M_{\rm low}$, which we choose as a free parameter. In these analytic estimates, clustering is usually treated with simple linear models in which the long-wavelength cluster distribution is amplified over the underlying mass distribution by a mass-dependent biasing factor, leading to a power spectrum $b(M_1)b(M_2)P(k)$ amplified over the underlying dark matter spectrum $P(k)$. This turns out to be a small effect for the SZ power spectra.

To describe the gas profile, we need the pressure profile. We take it to be that for an isothermal distribution with a baryon density profile given by a β-model with $\beta = 2/3$. For the gas temperature, we adopt the virial theorem relation given in Pen (1998b): $M/M_8 = (T/T_8)^{3/2}$, where M_8 is the mean mass contained in an $8\ h^{-1}$ Mpc sphere and $T_8 = 4.9\Omega_m^{2/3}\Omega(z)^{0.283}(1+z)$ keV, where $\Omega(z)$ is the fraction of matter density with respect to the critical density at redshift z. This relation was obtained by comparing the gas temperature distribution in simulations with the halo mass function described above. For the electron number density profile we adopt $n_e = n_{e0}(1 + r^2/r_{\rm core}^2)^{-1}$, scaled by the central density n_{e0} and core radius $r_{\rm core}$. Since our simulations show that the pressure profile falls off more rapidly than the product of temperature and density given here would indicate, we truncate the pressure at a fraction $fr_{\rm vir}$ of the virialized radius $r_{\rm vir}$. The virial radius is defined as the radius of a sphere with mass M and mean density $\Delta_c(z)\bar{\rho}(z)$, where $\bar{\rho}(z)$ is the mean matter density at redshift z and Δ_c is given by Eke et al. (1996). If we assume that gas accounts for a fraction Ω_B/Ω_m of the halo mass, the baryon content fixes one of the three parameters, n_{e0}. We treat f and $r_{\rm vir}/r_{\rm core}$ as free parameters to be fitted to the SZ power spectrum.

Figure 6 (*bottom*) shows typical fits that we can obtain with the above model using $r_{\rm vir}/r_{\rm core} = 4.8$ and $f = 0.9$. Given the number of free parameters, many combinations of values can yield reasonable fits. In order to investigate the resolution effects in our simulations, we fix $r_{\rm vir}/r_{\rm core}$ and f and vary the lower mass cutoff $M_{\rm low}$ and the k-range cutoff in the analytic model. These parameters are related to the resolution limitations of our simulations. For the MMH simulation, we find that the effect of the k-range cutoff is negligible, but that $M_{\rm low}$ has a larger effect. Since we need more than 100 gas and dark matter particles to resolve a halo, we choose $M_{\rm low}$ as the mass of 100 gas particles and 100 dark matter particles. This corresponds to $0.0015M_8$ for the 512^3 simulation. We see substantial deviations developing when $M_{\rm low} > 0.01M_8$. There are as well other uncertainties not included in our hydrodynamic simulations, which are adiabatic. For example, the outflow of gas from groups could lead to an effective mass cutoff that is physical rather than resolution dependent. The concentration parameter for gas, $r_{\rm vir}/r_{\rm core}$, could be a function of mass and of redshift, which would also change the results.

4. SIMULATING CBI OBSERVATIONS OF THE SUNYAEV-ZEL'DOVICH EFFECT

The estimation of band powers used in the analysis of the CBI observation is based on a maximum likelihood technique that assumes the signal to be a Gaussian random field (Paper IV). This assumption appears to be justified in the case of primary CMB anisotropies, where no clear evidence of non-Gaussianity has been found. However, the contributions from various foregrounds are non-Gaussian. Although the observations are noise dominated at the scales of interest for the CBI deep field excess and therefore are expected to be predominantly Gaussian, it is important to test the effect of a small non-Gaussian signal such as an SZ foreground on the band power estimation procedure.

We used the simulated SZ maps to test the effect of an SZ foreground on the CBI analysis pipeline. To do this, we constructed detailed mock data sets using the CBI simulation tools (Paper IV). We took real observations for particular dish configurations and pointings and replaced the observed visibilities by realizations of the expected signal and instrumental noise. This resulted in simulated observations with u-v coverage identical with the actual observations. The simulations can also include foreground templates as a distribution of point sources or maps of the SZ effect.

Each simulated $2^\circ \times 2^\circ$ SZ map is used as a foreground and added to a primary CMB background to generate mock observations of the $08^{\rm h}$ deep field. One point to note is that the CBI observations are actually differenced to minimize any ground pickup (Paper II). This involves subtracting the signal from two fields ("lead" and "trail") separated by 8 minutes of right ascension on the sky. In adding an SZ foreground to the simulated observations, two separate SZ maps were used as lead and trail fields. For this exercise, we created 20 simulated observations using the 40 MMH maps and 10 using the 20 SPH maps.

The mock data sets were then processed through our power spectrum estimation pipeline, as described in Paper IV. The maximum likelihood calculation of the power spectrum used template correlations to project out the expected contribution from point-source foregrounds. Since point-source templates were projected out of the data or were constrained at a known amplitude (as in the case of the residual unresolved background), the power

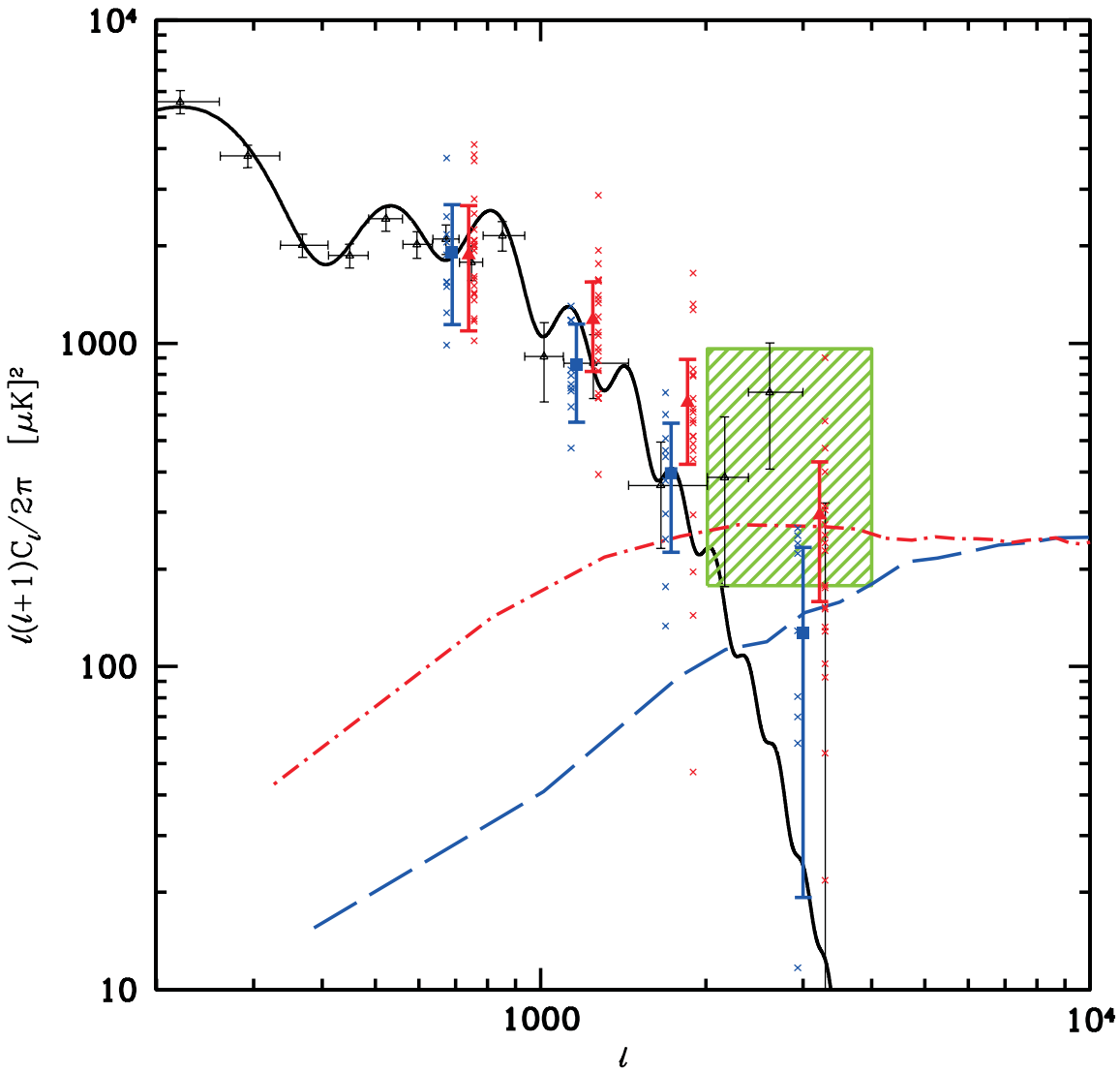

FIG. 7.—Simulated observations of CMB plus SZ fields. The result of band power estimation on simulated observations of the 08^h deep field containing noise, realizations of a fiducial ΛCDM model shown in black (*solid line*), and SZ foregrounds from the SPH and MMH $\sigma_8 = 1.0$ simulations. The blue (*dashed*) curve shows the average power spectrum of the input SPH maps, and the red (*dash-dotted*) curve is the average power spectrum of the input MMH maps. The red (*triangle*) points are the average band powers obtained from the analysis of 20 separate observations using the MMH maps. The blue (*square*) points are the average band powers obtained from 10 SPH maps. The band power estimation pipeline recovers the correct power in the SZ-dominated region $l > 2000$. The green (*hatched*) rectangle shows the 95% confidence region for the high-l CBI deep field result. Both the MMH and SPH codes show power consistent with the confidence region.

in the excess was assigned to the CMB when fitting for the band powers, since no other correlations were included in the quadratic power spectrum estimator (except for instrumental noise). We reproduced this situation by simulating observations of primary CMB realizations with SZ foregrounds, but only allowing for noise and CMB contributions to the total correlation matrix in the likelihood

$$\mathbf{C} = \mathbf{C}^N + \mathbf{C}^{\rm CMB}, \tag{3}$$

where the correlations due to the CMB are expressed as a function of the band power $\mathcal{C}_B$ with

$$\mathbf{C}^{\rm CMB} = \sum_B \mathcal{C}_B \frac{\partial \mathbf{C}^{\rm CMB}}{\partial \mathcal{C}_B}. \tag{4}$$

The SZ maps were produced from simulations of different cosmologies, and we have shown how the spectra can be scaled to fiducial $\Omega_b h$ and σ_8 values for comparison. However, when simulating the measurement of band powers, we chose to use unscaled contributions in order to test the different amplitude regimes given by the different values of baryon density. As a primary CMB signal, we used random realizations of a single ΛCDM model ($\Omega_m = 0.30$, $\Omega_b = 0.04$, $\Omega_\Lambda = 0.70$, $h = 0.68$, and $n_s = 0.975$). For the SZ contributions, we restricted ourselves to the $\sigma_8 = 1.0$ simulations.

Results are shown in Figure 7. The band powers are averaged over the 20 and 10 independent realizations from the two $\sigma_8 = 1.0$ simulations. The triangles are for the MMH simulations, and the SPH results are shown as squares. The model used for the primary CMB contribution is also shown, together with the 2 σ confidence region for the deep excess. The errors shown are obtained from the variance of the measured band powers. The averages appear to recover the input power accurately in both regimes in which either the primary CMB signal or the SZ signal dominates.

The interpretation of the errors is of course complicated in the SZ-dominated regime by the non-Gaussianity of the SZ signal

(e.g., Zhang et al. 2002). The small area considered in the simulations results in significant sample variance effects in the measurements of the SZ power. The scatter in the observed band powers over the different realizations is also shown in Figure 7. The non-Gaussian scatter is significant, although this effect would decrease for the larger area probed in the joint three-field analysis and because the high-l errors are dominated by the noise. It is also important to note that if the SZ effect is a significant source of the power in the observations, the sample variance component of the errors derived in the optimal spectrum estimation would be biased.

It is also interesting to note the effect of the low-l contribution in the MMH simulations. There is a sizable contribution to the band powers below $l \sim 2000$. Although this effect may be due to the presence of one rather large cluster in the simulation, as discussed above, it raises the question of whether an SZ signal with high enough amplitude to explain the excess may already be constrained by its low-l contributions.

5. WIENER-FILTERING THE CBI DEEP FIELD OBSERVATIONS

The CBI does not have sufficient frequency coverage to strongly distinguish different signals by their frequency dependence (e.g., CMB, SZ, and Galactic foregrounds). Spectral separation of the different components is therefore infeasible. Although the sensitivity of the CBI results presented here is not sufficient to conclusively identify individual features in the maps, we present examples and simulations of a Wiener-filtering technique described in Paper IV.

The total mode-to-mode correlations in the data are separated into four components in a typical analysis of the deep field visibilities, with the weight matrix $\mathbf{W}$ as the sum

$$\mathbf{W} = \left(\mathbf{C}^{N} + \mathbf{C}^{\mathrm{CMB}} + \mathbf{C}^{\mathrm{SRC}} + \mathbf{C}^{\mathrm{res}}\right)^{-1}, \tag{5}$$

with noise (N), CMB, known source (SRC), and residual source (res) components, respectively. (In Papers II and III, the known source contribution is split into two components, for sources with and without measured flux densities.)

In the limit at which all the components can be considered Gaussian random fields, we can define the probability of each signal given the data as the Gaussian (Bond & Crittenden 2001)

$$\ln P\left(\Delta^{\mathrm{X}}|\bar{\Delta}\right) = -\frac{1}{2}\left(\Delta^{\mathrm{X}} - \left\langle \Delta^{\mathrm{X}}\middle|\bar{\Delta}\right\rangle\right)^{\dagger}\left(\mathbf{C}^{\mathrm{X}}\right)^{-1}\left(\Delta^{\mathrm{X}} - \left\langle \Delta^{\mathrm{X}}\middle|\bar{\Delta}\right\rangle\right) - \frac{1}{2}\mathrm{Tr}\ln\mathbf{C}^{\mathrm{X}} - N\ln\sqrt{2\pi}, \tag{6}$$

where $\bar{\Delta}$ are the observations, Δ^{X} is the map vector of the component X, $\mathbf{C}^{\mathrm{X}}$ is the mode-to-mode correlation matrix for the component, N is the number of modes in the map, and the dagger symbol indicates the Hermitian conjugate. The mean $\langle\Delta^{\mathrm{X}}|\bar{\Delta}\rangle$ defines the Wiener-filtered map of the component given the observations

$$\Delta^{\mathrm{X}} = \mathbf{C}^{\mathrm{X}}\mathbf{W}\bar{\Delta}, \tag{7}$$

with variance about the mean

$$\left\langle \delta\Delta^{\mathrm{X}}\delta\Delta^{\mathrm{X}\dagger}\middle|\bar{\Delta}\right\rangle = \mathbf{C}^{\mathrm{X}} - \mathbf{C}^{\mathrm{X}}\mathbf{W}\mathbf{C}^{\mathrm{X}}. \tag{8}$$

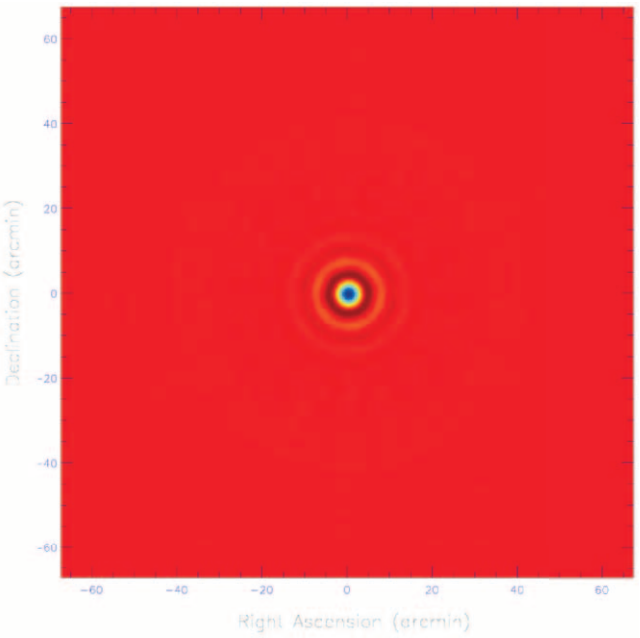

FIG. 8.—Image produced by gridding a simulated observation of a point source placed at the center of the 08^{h} field.

In our case, the maps Δ are column vectors containing the gridded visibility estimators (Paper IV), and sky plane maps can be obtained by fast Fourier transforming these estimators in the u-v plane. The correlation structure of the estimator grids is a necessary by-product of our gridding method and power spectrum estimation pipeline. The calculation of the correlations includes all the relevant information on the sampling structure and the convolution of the fine-grained observation plane. Equation (8) therefore includes all aspects of the uncertainties in the Wiener-filtered map resulting from the observations.

Because of the complex weighting applied to the observed visibilities in our gridding scheme, it is difficult to assign units to the maps produced by simply Fourier transforming the gridded u-v plane. In order to obtain images with approximate normalizations in units of mJy pixel^{-1}, we reweight by dividing the vector at each lattice site by a second vector obtained by gridding a 1 mJy point source placed at the center of each field. It is important to note that this deconvolution is carried out in the coarse-grained lattice and is not a full deconvolution of the effect of the dirty beam, since no extra information is added to complete the u-v plane when gridding. In Figure 8 we show the image obtained by Fourier transforming the gridded u-v plane of a simulated observation of a point source placed at the center of the 08^{h} field.

We show an example of the use of such filters in Figure 9. The sequence shows the result of applying different filters to the 08^{h} deep field observation. The original image (*top left*) is first filtered to obtain a map of the total signal contributions, which includes CMB and point sources (*top right*). The CMB power spectrum obtained from the joint deep field analysis is then used as a template to obtain a map of the CMB contribution (*bottom left*). The template includes the excess power above $l \sim 2000$. The postsubtraction residuals in the known point sources can also be separated into an image (*bottom right*) that shows the total contribution of the modes that are projected out when estimating the power spectrum. The mean Wiener-filtered maps make no statement on the significance of any feature by themselves, and considering only the mean can be misleading, since

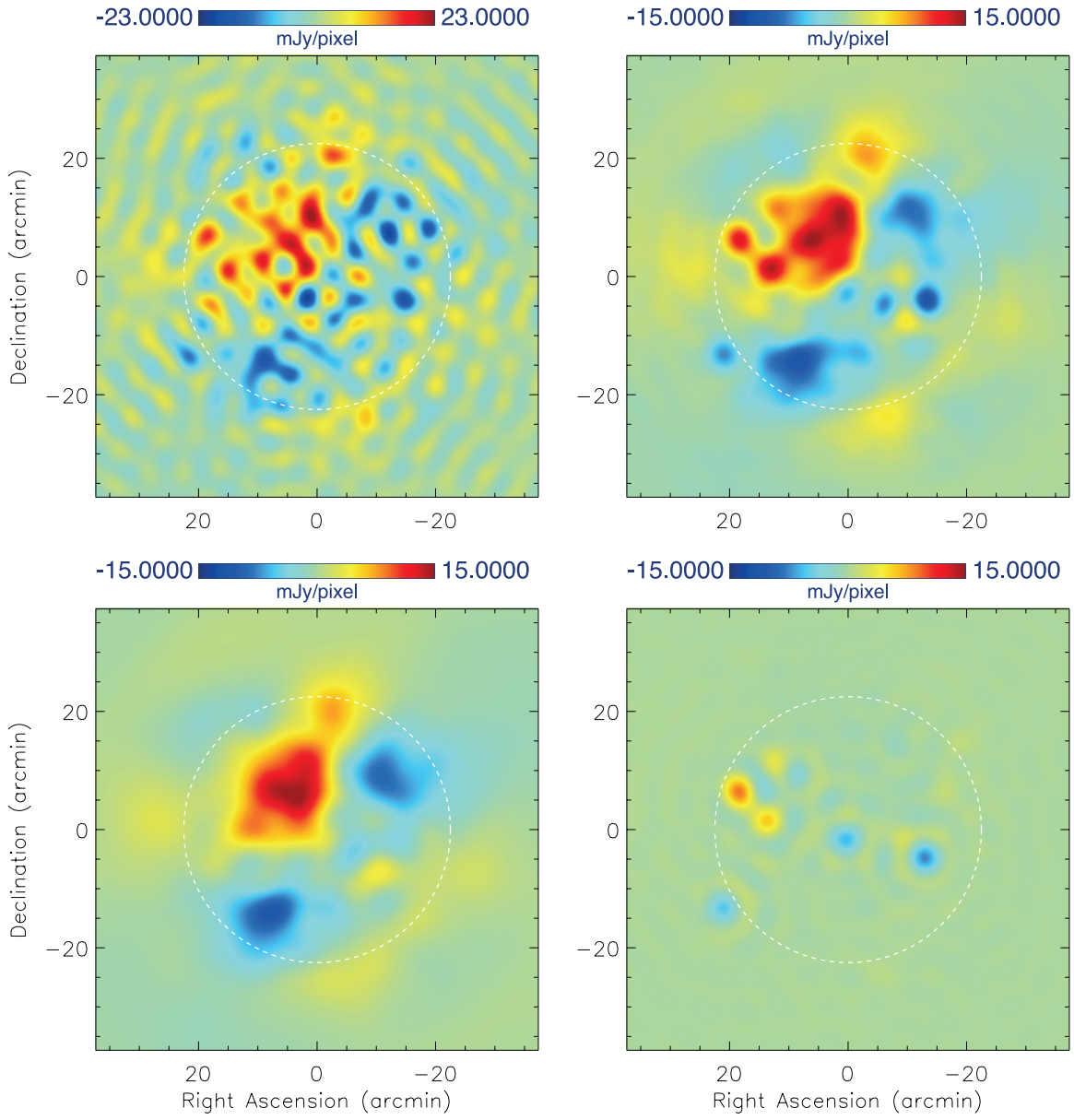

FIG. 9.—Filtered images of the CBI 08^h deep field. The total signal plus noise image (*top left*) displayed as a $70' \times 70'$ field. The white (*dashed*) circle shows the $45'$ FWHM of the primary beam. A total signal image (*top right*) is obtained by using the sum of CMB and point-source foreground correlations as a template. The amplitude of the residual source background is set to a flux of 0.08 $\mathrm{Jy^2\ sr^{-1}}$ in the filter. Using the joint deep field band powers as amplitudes in the filters, we obtain the optimal image for the CMB (*bottom left*). This image encompasses the power attributed to the high-l excess. The known point-source residuals can also be filtered out of the data (*bottom right*). Color scales are kept constant for the filtered images to ease comparison of the relative amplitudes of the components. The images are deconvolved by the response of a simulated source placed at the center of the field.

there is no information on the allowed fluctuations around the mean in the map itself. This is particularly so in the case of interferometric observations, where the nature of the noise and sampling uncertainties means that, although the power due to single features is conserved, their structure in the sky plane is complicated by the extended nature of the correlations in the uncertainties. As shown above, however, in the Gaussian limit we can assign confidence limits to any feature using equation (8).

A useful method of visualizing the significance of the features is by creating constrained realizations of the fluctuations and comparing these to the mean. For example, we can obtain a random realization of the fluctuations by taking $\Delta_i^{\mathrm{X}} = (\mathbf{C}^{\mathrm{X}} - \mathbf{C}^{\mathrm{X}}\mathbf{W}\mathbf{C}^{\mathrm{X}})^{1/2}\xi$, where ξ are random Gaussian variates with unit norm. By adding these maps to the mean, we get an idea of the allowed fluctuations about the mean. Strongly constrained features are relatively unaffected by the fluctuations and represent the high signal-to-noise ratio limit, where $\mathbf{C}^{\mathrm{X}} - \mathbf{C}^{\mathrm{X}}\mathbf{W}\mathbf{C}^{\mathrm{X}} \rightarrow 0$. Features measured at levels comparable to the generalized noise of the observations are washed out by the fluctuation levels and represent the limit $\mathbf{C}^{\mathrm{X}} - \mathbf{C}^{\mathrm{X}}\mathbf{W}\mathbf{C}^{\mathrm{X}} \rightarrow \mathbf{C}^{\mathrm{X}}$. The full pixel-pixel covariance matrix of the component map can be calculated by direct fast Fourier transformation of the covariance matrix or by taking Monte Carlo ensemble averages of the fluctuation realizations.

The level of fluctuations allowed around the mean for the CMB component of Figure 9 is shown in Figure 10. This figure shows the Wiener filter of the component and the same map with three random realizations of the fluctuations added to it. As expected, the CMB component is well constrained on the scales shown in the image, since the signal-to-noise ratio is high: i.e.,

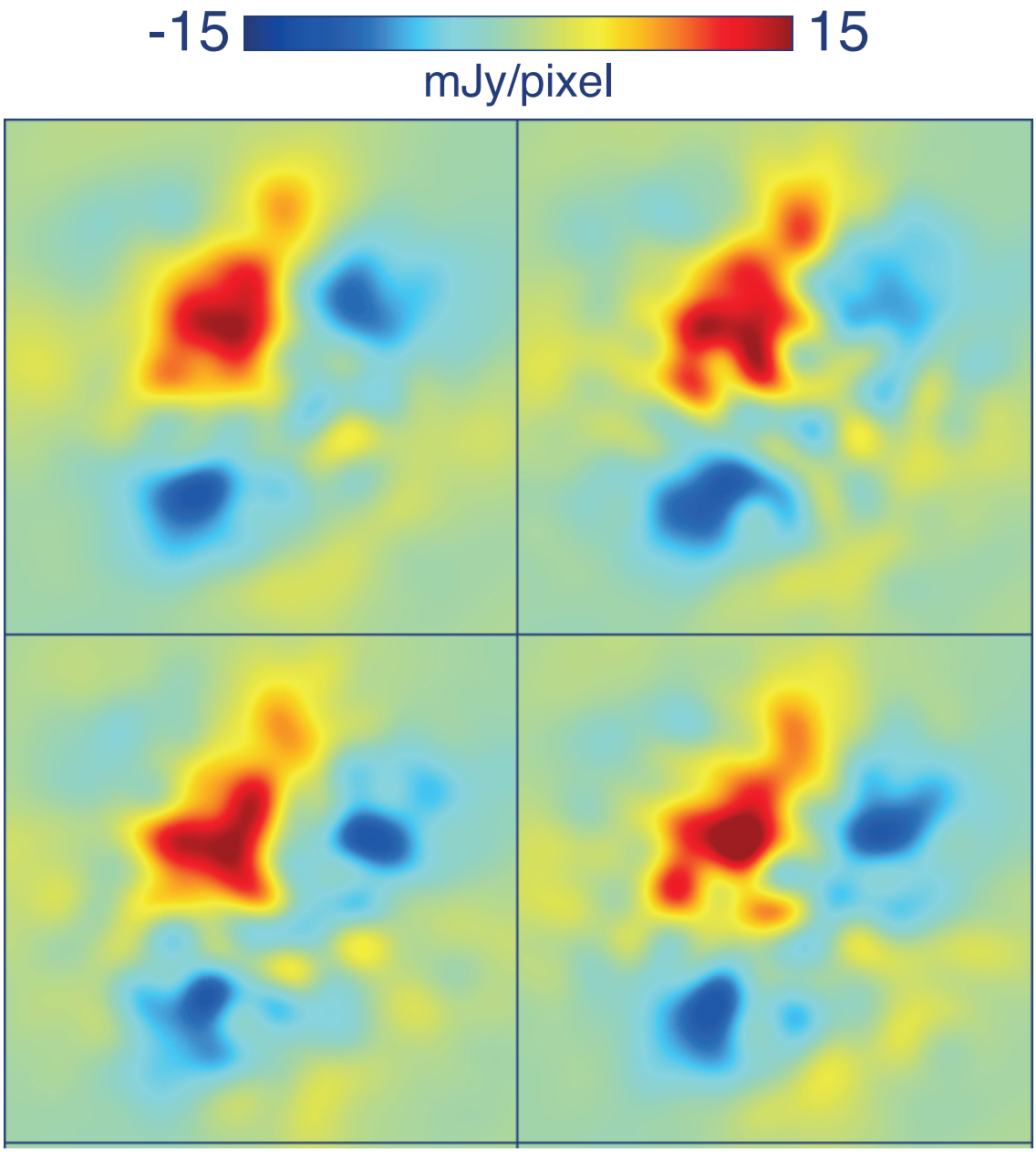

FIG. 10.—Another way to illustrate whether the features seen in the Wiener-filtered images are robust: show a few fluctuations about the mean (Wiener) map, here for the 08^h deep field. The top left panel reproduces the mean CMB component map of Fig. 9. The remaining three panels show the addition of three constrained realizations of the allowed fluctuations to the mean map. At the signal-to-noise ratios of the larger scale CMB observations, the features are robust to the fluctuations. Note that these images are dirty maps: no attempt has been made to compensate for gaps in the u-v coverage. The features are a combination of main lobe and sidelobe responses to the CMB.

the main features in the map are stable with respect to the fluctuations. The features are therefore expected to be closely related to "real" structures on the sky, but the nature of the observations, in particular the sidelobes of the point-spread function (synthesized beam), means that the detailed structure of the features is not well constrained and most likely does not reflect the precise shape of the objects. The filtering of the large-scale power by the interferometric observations also makes the correspondence with the large-scale features on the sky not as intuitive as with sky plane–based measurements.

Using the specific SZ models that we introduced in § 4, we can now extend the image analysis by template-filtering the images specifically for SZ contributions. As described above, the only components modeled in the total correlation matrix are the CMB, instrumental noise, and source components. We therefore construct the SZ template as

$$\mathbf{C}^{\rm SZ} = \sum_B \mathcal{C}_B^{\rm SZ} \frac{\partial \mathbf{C}^{\rm CMB}}{\partial \mathcal{C}_B}, \tag{9}$$

where the amplitudes $\mathcal{C}_B^{\rm SZ}$ are obtained by filtering the average SZ power spectra by the deep field band window functions (see Paper II).

The resulting SZ-filtered images should reproduce the structure in input SZ maps, and we find that this is indeed the case. The sequence of images in Figure 11 is an example of the filtering for one of the SPH maps (*top*) and one of the MMH maps

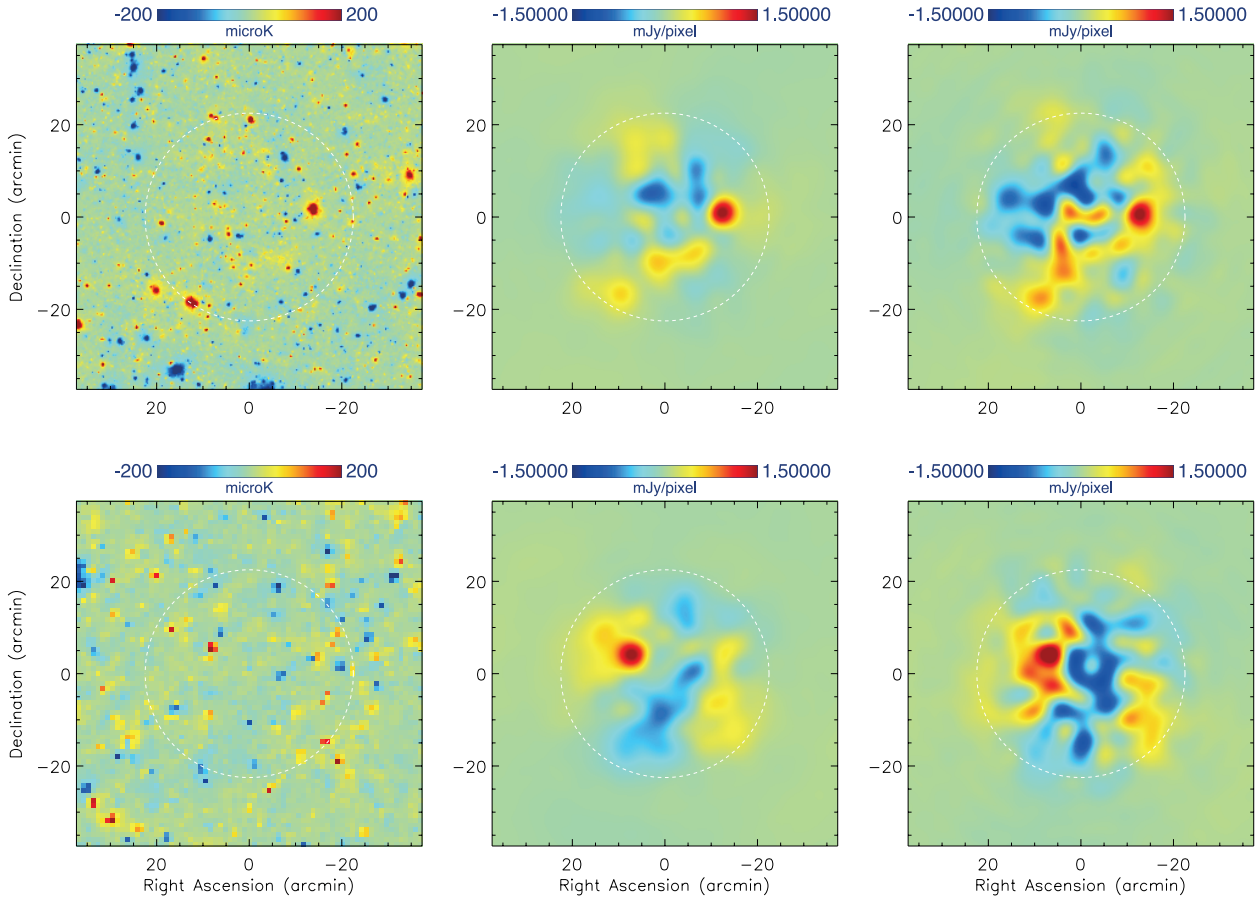

FIG. 11.—Simulated observations of SZ signals. A single SZ realization is shown for the SPH (*top left*) and MMH (*bottom left*) simulations. The area represents a lead minus trail differenced field used as the signal in a simulated observation of the 08^h deep field. The maps are used to generate mock data sets with exact replications of the *u-v* coverage of the real data, which are then filtered using the respective SZ templates. Mock data sets with close to negligible noise levels (*middle, top and bottom*) show the direct representation of the CBI processed input maps. The same realization but with the same noise levels as the observed data is shown in the top and bottom right panels. To within the accuracy allowed by the noise, the filtered images successfully reproduce the features of the input maps within the primary beam area.

(*bottom*). The left-hand panels show the input SZ maps (lead minus trail), and the middle ones show the result of filtering mock data sets in which the noise has been reduced to negligible levels. These provide a control set to compare with the reconstructed noisy observations (*right*). The strongest features in both images reproduce the strongest SZ signatures in the input templates, although one has to take into account the tapering effect induced by the primary beam when comparing the input maps to the filtered data (see Paper IV). The tapering suppresses the amplitude of significant features further out in the beam with respect to those close to the center of the field. The noise level is such that the significance of the detections is not obvious. These can be quantified by comparing with the allowed fluctuations about the mean Wiener filter (eq. [8]).

We have also applied the SZ Wiener filter to the deep field data itself. These SZ-filtered images scale linearly with the overall normalization of the SZ power spectrum. Hence, by calibrating the SZ template filters with the observed deep high-l power, we can obtain an image with the same signal-to-noise ratio as in the observations. In Figure 12, we show the effect of the SZ filter on the data split in two roughly equal halves for the 08^h and 20^h deep field observations. When comparing the two halves, the noise is uncorrelated, so any common stationary signal of sufficient amplitude should appear in both halves. One sees no obvious strong signal-dominated stationary features, but there is one in each field, albeit with amplitudes comparable to the noise fluctuations. We conclude that the images are noise dominated and that there are no obvious features that could singlehandedly account for the observed excess. This is in agreement with the excess being a statistical measurement, as opposed to a high signal-to-noise observation.

6. DISCUSSION

We have presented estimates for the possible contribution from the SZ effect to the CBI deep field observations, which show evidence of an excess in power over standard primary CMB scenarios above $l \sim 2000$. Our numerical simulations show that an amplitude of $\sigma_8 \approx 1$ appears to give, on average, enough power in the SZ signature to explain the excess. Current primary CMB and LSS data favor models with somewhat lower normalizations: for flat, *HST–h*, and LSS priors, $\sigma_8 = 0.88 \pm 0.08$ for the 2002 June data set and $0.86^{+0.04}_{-0.03}$ for the 2003 March compilation. Recent weak-lensing–only results, e.g., 0.83 ± 0.07 (van Waerbeke et al. 2005), are also quite compatible with CMB-only values.

In assessing whether $\sigma_8 \approx 0.9$ is too low to explain the anomaly, the non-Gaussian nature of the sample variance of the SZ effect should be included. This issue has been partially addressed in the literature (Cooray & Sheth 2002; Springel et al. 2001; Komatsu & Seljak 2002). Goldstein et al. (2003) have shown that a joint analysis of our CBI deep field data with recent data from ACBAR (Kuo et al. 2004) and BIMA (Dawson et al. 2002) that simultaneously fits the amplitudes of the primary and SZ power

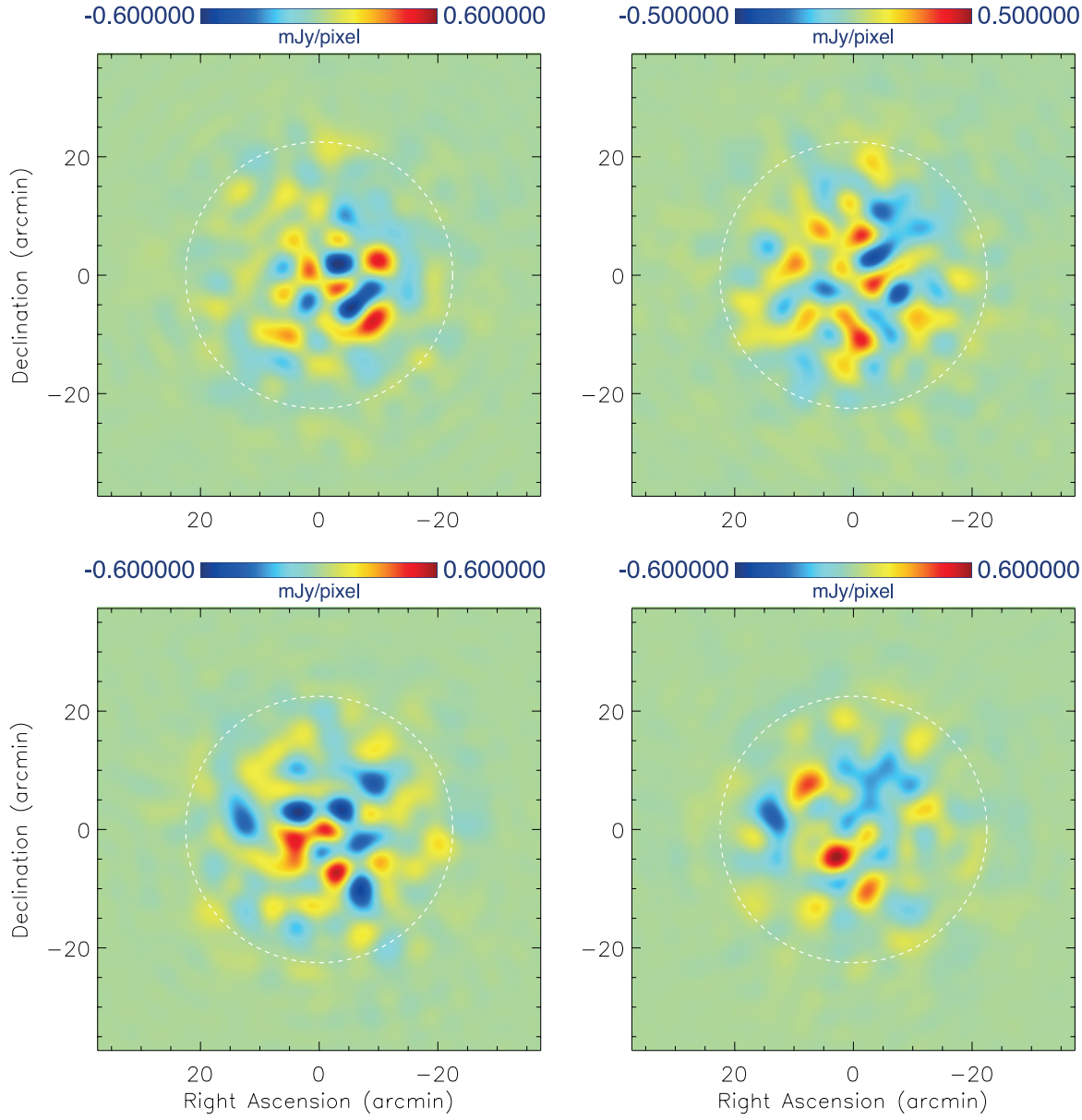

FIG. 12.—Split deep field data, Wiener-filtered with the SZ template, for the 08^h field (*top*) and the 20^h field (*bottom*). There is no clear evidence of a high signal-to-noise stationary feature.

spectra and roughly accounts for the non-Gaussianity of the SZ effect requires $\sigma_8 = 0.96^{+0.08}_{-0.16}$, with a maximum likelihood at 1.00, consistent with the constraints on σ_8 from primary CMB and LSS data, as illustrated in Figures 1 and 2. Readhead et al. (2004) applied a similar joint analysis to that in Goldstein et al. (2003) to the band powers of the ACBAR, BIMA, and CBI 2 yr data. An attempt to bracket the effects of non-Gaussianity was made by allowing the sample variance component of the error bar to increase by a factor of up to 4: the estimate of σ_8 hardly changed, going from $0.98^{+0.06}_{-0.07}$ to $0.98^{+0.06}_{-0.08}$. Goldstein et al. (2003) used a factor of 3 to estimate the non-Gaussian effect. A bigger impact is found at the 2 σ level: with a uniform prior in σ_8, there is a tail skewed to low σ_8, primarily because the amplitude being fitted by the analysis is σ_8^7 and the distribution is roughly Gaussian in that variable, as shown explicitly in Figure 12 of Readhead et al. (2004). We note that the errors are predominantly from noise and not sample variance for the CBI data, which is why variation by a factor of 4 does not have a huge effect.

The Goldstein et al. (2003) and Readhead et al. (2004) analyses took into account the competing effects of the damping tail of the primary CMB fluctuations and the rising SZ power spectrum over the entire l-range, not just in the $l > 2000$ regime, where the excess is clearly seen. The assumption is that the power spectra are described by an offset lognormal distribution, which has been shown to hold well for Gaussian signals and noise (Bond et al. 2000; Paper V). The distribution becomes a Gaussian one in the noise-dominated regime and a lognormal one in the signal-dominated regime. If the signal comes from clusters and groups, the latter will not be accurate, and further work is needed to properly assess the limits derived from the excess. What is needed is a full suite of Monte Carlo simulations, guided by semianalytic theory, to study the effects of non-Gaussianity, rather than reliance on expanded signal errors.

The excellent agreement among the runs using the two separate hydrodynamic algorithms is encouraging and lends support to the conclusions on the required normalization. We note that the simulations employed in this work were developed and

run independently from each other and the CBI analysis effort (Bond et al. 2002; Zhang et al. 2002). However, both simulations were adiabatic, with entropy increases occurring only by shock heating. The influence of cooling and entropy injection from supernovae, etc., on the predicted SZ spectrum remains to be explored, as does the effect of such technical issues as numerical convergence when the simulation resolution is changed.

The limited number of mock simulations that we have carried out show that our experimental setup does reproduce correctly the signal of simulated SZ foregrounds. This suggests that the Gaussian assumption implicit in our band power estimation procedures does not break down at the SZ signal-to-noise ratios of the deep field observations.

If the excess is not due to the SZ effect, what could be the cause? Other possible origins of the excess were addressed in Paper II. It is inconsistent with adiabatic inflationary predictions for primary anisotropies on the damping tail only at the $\sim 3\,\sigma$ level. The excess clearly needs to be further explored, both within the CBI data set itself and also by correlating with other observations of these deep fields. The statistical nature of the detected excess means we cannot identify single features responsible for the excess in the deep fields even after Wiener-filtering the data with SZ-derived templates.

Our principal conclusion is that the CBI excess could be a result of the SZ effect for the class of ΛCDM concordance models if σ_8 is in the upper range of values allowed by current CMB data. The simple $\mathcal{C}_l \propto \sigma_8^7(\Omega_b h)^2$ scaling (eq. [2]) shows that the lower σ_8 values preferred by the CMB data imply SZ signals below, but not too far below, the sensitivity obtained by the CBI deep observations. This work also highlights how the signature of the SZ effect has great potential for constraining the amplitude σ_8. The sensitive scaling of the CMB power with σ_8 results in significant constraints even with large errors on the observed band powers. This further underlines the significance of blank field observations at $l \gtrsim 2000$, which should reveal the SZ structure that necessarily lurks as a by-product of CMB-normalized structure formation models.

We thank Hugh Couchman, Tom Quinn, and Joachim Stadel for interactions regarding the computational issues. Research in Canada is supported by NSERC and the Canadian Institute for Advanced Research. The computational facilities (SHARCNET at McMaster and PSciNet at Toronto) are funded by the Canadian Fund for Innovation. This work was supported by the National Science Foundation under grants AST 94-13935, AST 98-02989, and AST 00-98734. We are grateful to CONICYT for granting permission to operate the CBI at the Chajnantor Scientific Preserve in Chile.

REFERENCES

Allen, S. W., Schmidt, R. W., Fabian, A. C., & Ebeling, H. 2003, MNRAS, 342, 287
Atrio-Barandela, F., & Mucket, J. 1999, ApJ, 515, 465
Bacon, D., Massey, R., Refregier, A., & Ellis, R. 2003, MNRAS, 344, 673
Bahcall, N. A., & Fan, X. 1998, ApJ, 504, 1
Bardeen, J. M., Bond, J. R., Kaiser, N., & Szalay, A. S. 1986, ApJ, 304, 15
Birkinshaw, M., Gull, S. F., & Hardebeck, H. 1984, Nature, 309, 34
Bond, J. R. 1988, in The Early Universe, ed. W. G. Unruh & G. W. Semenoff (NATO ASI Ser. C, 219; Dordrecht: Kluwer), 283
———. 1994, in Relativistic Cosmology, ed. M. Sasaki (Tokyo: Universal Academy Press), 23
———. 1996, in Les Houches, Session LX, Cosmology and Large Scale Structure, ed. R. Schaeffer, J. Silk, M. Spiro, & J. Zinn-Justin (Amsterdam: Elsevier), 469
Bond, J. R., Contaldi, C. R., & Pogosyan, D. 2003, Philos. Trans. R. Soc. London A, 361, 2435
Bond, J. R., & Crittenden, R. G. 2001, in Structure Formation in the Universe, ed. R. G. Crittenden & N. G. Turok (NATO ASI Ser. C, 565; Dordrecht: Kluwer), 241
Bond, J. R., & Efstathiou, G. 1987, MNRAS, 226, 655
Bond, J. R., & Jaffe, A. H. 1999, Philos. Trans. R. Soc. London A, 357, 57
Bond, J. R., Jaffe, A. H., & Knox, L. 2000, ApJ, 533, 19
Bond, J. R., Kofman, L., Pogosyan, D., & Wadsley, J. 1998, in IAP Colloq. 14, Wide Field Surveys in Cosmology, ed. S. Colombi, Y. Mellier, & B. Raban (Paris: Editions Frontières), 17
Bond, J. R., & Myers, S. 1996, ApJS, 103, 1
Bond, J. R., Ruetalo, M. I., Wadsley, J. W., & Gladders, M. D. 2002, in ASP Conf. Ser. 257, AMiBA 2001: High-*z* Clusters, Missing Baryons, and CMB Polarization, ed. L.-W. Chen, C.-P. Ma, K.-W. Ng, & U.-L. Pen (San Francisco: ASP), 15
Borgani, S., et al. 2001, ApJ, 561, 13
Brown, M., Taylor, A., Bacon, D., Gray, M., Dye, S., Meisenheimer, K., & Wolf, C. 2003, MNRAS, 341, 100
Carlberg, R. G., Morris, S. L., Yee, H. K. C., & Ellingson, E. 1997, ApJ, 479, L19
Carlstrom, J. E., Joy, M., & Grego, L. 1996, ApJ, 456, L75
Cole, S., & Kaiser, N. 1988, MNRAS, 233, 637
Cooray, A. 2000, Phys. Rev. D, 62, 103506
Cooray, A., & Sheth, R. 2002, Phys. Rep., 372, 1
Dawson, K. S., Holzapfel, W. L., Carlstrom, J. E., LaRoque, S. J., Miller, A., Nagai, D., & Joy, M. 2002, ApJ, 581, 86
Dodelson, S., et al. 2002, ApJ, 572, 140
Efstathiou, G., Bond, J. R., & White, S. D. M. 1992, MNRAS, 258, 1P (EBW92)
Eke, V. R., Cole, S., & Frenk, C. S. 1996, MNRAS, 282, 263
Goldstein, J., et al. 2003, ApJ, 599, 773
Grainge, K., Grainger, W. F., Jones, M. E., Kneissl, R., Pooley, G. G., & Saunders, R. 2002, MNRAS, 329, 890
Grainge, K., et al. 2003, MNRAS, 341, L23
Halverson, N. W., et al. 2002, ApJ, 568, 38
Hamana, T., et al. 2003, ApJ, 597, 98
Heymans, C., Brown, M., Heavens, A., Meisenheimer, K., Taylor, A., & Wolf, C. 2004, MNRAS, 347, 895
Hoekstra, H., Yee, H. K. C., & Gladders, M. D. 2002, ApJ, 577, 595
Holzapfel, W. L., Wilbanks, T. M., Ade, P. A. R., Church, S. E., Fischer, M. L., Mauskopf, P. D., Osgood, D. E., & Lange, A. E. 1997, ApJ, 479, 17
Jaffe, A. H., et al. 2001, Phys. Rev. Lett., 86, 3475
Jarvis, M., Bernstein, G. M., Fischer, P., Smith, D., Jain, B., Tyson, J. A., & Wittman, D. 2003, AJ, 125, 1014
Kogut, A., et al. 2003, ApJS, 148, 161
Komatsu, E., & Kitayama, T. 1999, ApJ, 526, L1
Komatsu, E., & Seljak, U. 2002, MNRAS, 336, 1256
Kuo, C. L., et al. 2004, ApJ, 600, 32
Lahav, O., et al. 2002, MNRAS, 333, 961
Lange, A. E., et al. 2001, Phys. Rev. D, 63, 042001
Lee, A. T., et al. 2001, ApJ, 561, L1
Makino, N., & Suto, Y. 1993, ApJ, 405, 1
Mason, B. S., Myers, S. T., & Readhead, A. C. S. 2001, ApJ, 555, L11
Mason, B. S., et al. 2003, ApJ, 591, 540 (Paper II)
Melchiorri, A., & Silk, J. 2002, Phys. Rev. D, 66, 041301
Miller, A. D., et al. 1999, ApJ, 524, L1
Molnar, S., & Birkinshaw, M. 2000, ApJ, 537, 542
Myers, S. T., et al. 2003, ApJ, 591, 575 (Paper IV)
Netterfield, C. B., et al. 2002, ApJ, 571, 604
Padin, S., et al. 2001, ApJ, 549, L1 (Paper I)
Peacock, J. A., et al. 2001, Nature, 410, 169
Pearson, T. J., et al. 2003, ApJ, 591, 556 (Paper III)
Peebles, P. J. E., & Yu, J. T. 1970, ApJ, 162, 815
Pen, U.-L. 1998a, ApJS, 115, 19
———. 1998b, ApJ, 498, 60
———. 1998c, ApJ, 504, 601
Pierpaoli, E., Borgani, S., Scott, D., & White, M. 2003, MNRAS, 342, 163
Pierpaoli, E., Scott, D., & White, M. 2001, MNRAS, 325, 77
Press, W. H., & Schechter, P. 1974, ApJ, 187, 425
Readhead, A. C. R., et al. 2004, ApJ, 609, 498
Refregier, A., Rhodes, J., & Groth, E. J. 2002, ApJ, 572, L131
Reiprich, T. H., & Böhringer, H. 2002, ApJ, 567, 716
Ruhl, J. E., et al. 2003, ApJ, 599, 786
Schuecker, P., Böhringer, H., Collins, C. A., & Guzzo, L. 2003, A&A, 398, 867
Scott, P. F., et al. 2003, MNRAS, 341, 1076

Seljak, U. 2002, MNRAS, 337, 769
Seljak, U., Burwell, J., & Pen, U.-L. 2001, Phys. Rev. D, 63, 063001
Sievers, J. L., et al. 2003, ApJ, 591, 599 (Paper V)
Silk, J. 1968, ApJ, 151, 459
Spergel, D. N., et al. 2003, ApJS, 148, 175
Springel, V., White, M., & Hernquist, L. 2001, ApJ, 549, 681 (erratum 562, 1086)
Sugiyama, N. 1995, ApJS, 100, 281
Sunyaev, R. A., & Zel'dovich, Ya. B. 1970, Ap&SS, 7, 3
Szalay, A. S., et al. 2003, ApJ, 591, 1
Udomprasert, P. S., Mason, B. S., Readhead, A. C. S., & Pearson, T. J. 2004, ApJ, 615, 63
van Waerbeke, L., Mellier, Y., & Hoekstra, H. 2005, A&A, 429, 75
van Waerbeke, L., Mellier, Y., Pello, R., Pen, U.-L., McCracken, H. J., & Jain, B. 2002, A&A, 393, 369
Verde, L., et al. 2002, MNRAS, 335, 432
Viana, P. T. P., Nichol, R. C., & Liddle, A. R. 2002, ApJ, 569, L75
Voevodkin, A., & Vikhlinin, A. 2004, ApJ, 601, 610
Wadsley, J. W., Stadel, J., & Quinn, T. 2004, NewA, 9, 137
Zhang, P. J., Pen, U.-L., & Wang, B. 2002, ApJ, 577, 555